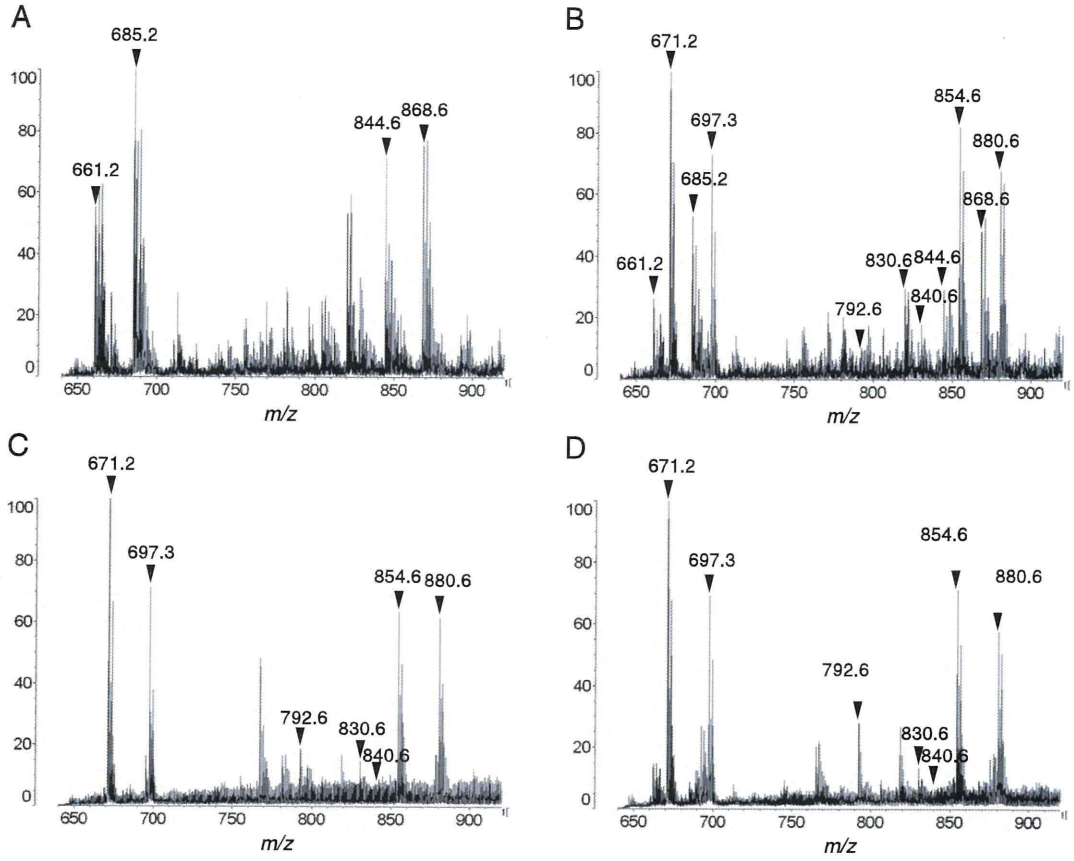

Fig. 5. HIGA-specific lipids are derived from urine. MALDI-QJT-TOF-MS-analyzed mass peaks of lipids extracted from control kidney (A), HIGA kidney (B), control urine (C), and HIGA urine (D) are shown. HIGA-specific mass peaks are seen in both the HIGA and control urine, while the mass peaks that are common in both kidneys are absent in urine.

oxygen atom and a saturation of the side chain. These findings suggest that these molecules may have a novel, unidentified renal function.

Although, we were unable to determine the chemical structures of 4 specific molecules corresponding to *m/z* 854.6, *m/z* 856.6, *m/z* 880.6, and *m/z* 882.6, tandem MS still provided some interesting findings. First, the fragments of *m/z* 854.6 and *m/z* 856.6 always had a difference of 2 Da, which was also true for *m/z* 880.6 and *m/z* 882.6. Second, *m/z* 854.6 and *m/z* 880.6, as well as *m/z* 856 and *m/z* 882 generated several common fragments. Third, PC(O-16:0/22:6) and PC(O-18:1/22:6) had a difference of 26 Da, while *m/z* 854.6 (or *m/z* 856.6) and *m/z* 880.6 (or *m/z* 882.6) also had one. Collectively, the results suggested that these lipids have common structural skeletons. In addition, *m/z* 854.6, *m/z* 856.6, *m/z* 880.6, and *m/z* 882.6 were speculated to be related to PC(O-16:0/22:6) and PC(O-18:1/22:6).

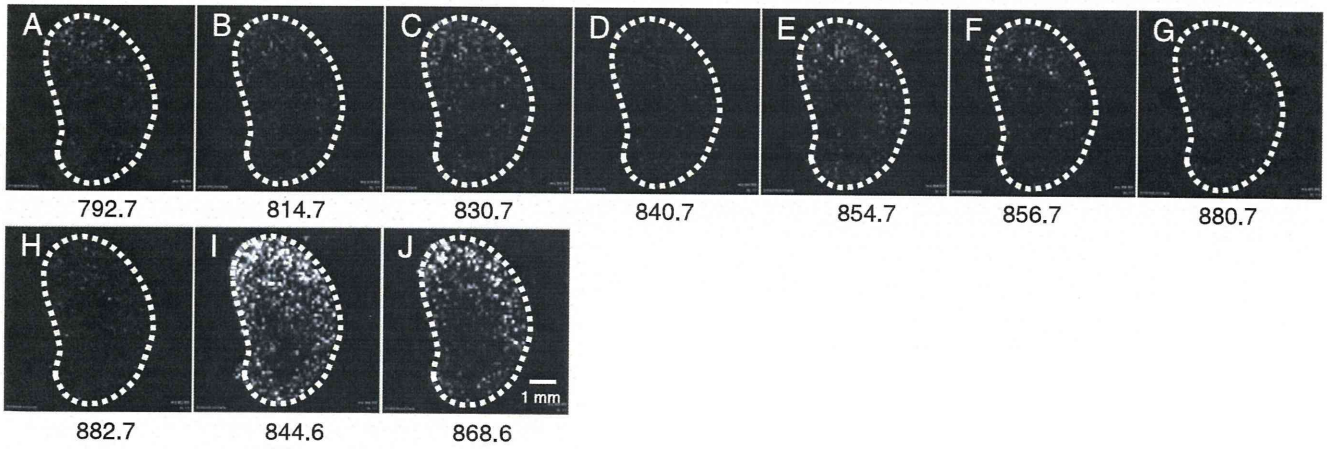

Fig. 6. Artificial urinary stagnation causes HIGA-specific distribution of lipids in tubular area. HIGA-specific mass peaks were detected in the kidneys of a unilateral urethral obstruction model (UUO) in which urine was artificially stagnated (A–H). Images of common mass peaks, *m/z* 844.6 and *m/z* 868.6, are also shown for comparison (I,J). Scale bar indicates a length of 1 mm.

Table 1
Distribution of identified lipid molecules in the kidney.

m/z	Distribution	Specificity	Molecules	Urine
844.6	Cortex	Common	[PC(16:0/22:6) + K]+	
868.6	Cortex	Common	[PC(18:2/22:6) + K]+	
879.7	Hilum	Common	[TAG(16:0/18:2/18:1) + Na]+	
905.9	Hilum	Common	[TAG(18:1/18:2/18:1) + Na]+	
792.6	Medulla	HIGA-specific	[PC(O-16:0/22:6) + H]+	Yes
814.6	Medulla	HIGA-specific	[PC(O-16:0/22:6) + Na]+	Yes
830.6	Medulla	HIGA-specific	[PC(O-16:0/22:6) + K]+	Yes
840.6	Medulla	HIGA-specific	[PC(O-18:1/22:6) + Na]+	Yes
854.6	Medulla	HIGA-specific	Not determined	Yes
856.6	Medulla	HIGA-specific	Not determined	Yes
880.6	Medulla	HIGA-specific	Not determined	Yes
882.6	Medulla	HIGA-specific	Not determined	Yes

The lesions in the tubular areas of HIGA mouse have been recognized but not well investigated. One of the reasons for this lack of investigation is that the lesions have not been considered a primary defect in IgA nephropathy in human diseases (Coppo et al., 2010). Another reason is absence of a technique that could identify the molecules. In this study, we detected molecular differences between HIGA and Balb/c mice. These findings could be associated with the histological differences that we have already indicated.

We also revealed that HIGA-specific lipids distributed in the tubular area are derived from urine and succeeded in reproducing the same findings by artificial urinary stagnation using the UUO model; this suggests that urinary stagnation causes HIGA-specific distribution. Urinary stagnation seems not to be the primary cause of IgA because it seems unrelated to glomerular lesions. This finding suggests that urinary stagnation and deposition of these molecules in the tubular area could affect the pathogenesis of the nephropathy and could be a clue for understanding other pathologic mechanisms such as acute renal failure.

Although we now have a better understanding of the mechanisms underlying the HIGA-specific molecular distribution of lipids in the kidney, the following issues need to be investigated: determination of the unidentified molecules, understanding the excretion system of lipids in urine, and discovery of the molecular differences in glomerular lesions of IgA nephropathy. Moreover, PC(O-16:0/22:6) and PC(O-18:1/22:6) are also known as analogues of platelet-activating factor (PAF) and a plasmalogen, respectively, and it will be worth investigating whether these molecules are related to the pathogenesis in IgA nephropathy (Coppo et al., 2010; Robinson et al., 1988).

Conclusion

In conclusion, our data are the first report that sheds light on the molecular distribution of lipids in the HIGA mouse kidney. In addition, IMS might provide the dynamic physiological function of kidneys in addition to the distributional information so that it might be applied to understanding the pathophysiology of various diseases.

Supplementary materials related to this article can be found online at doi:10.1016/j.yexmp.2011.07.002.

Conflict of Interest statement

The authors declare that there are no conflicts of interest.

Sources of support

This work was partly supported by grants from the Ministry of Education, Culture, Sports, Science and Technology of Japan (SENTAN to M.S., KAKENHI 20591212 and KAKENHI 20790714); the Ministry of Health, Labour and Welfare of Japan (H20shinkouippan012, H20nanchiippan035, H20shinkouippan015 and H23shinkouippan018); the program of Research on Publicly Essential Drugs and Medical Devices of the Japan Health Science Foundation (KHC3333); and Takeda Science Foundation.

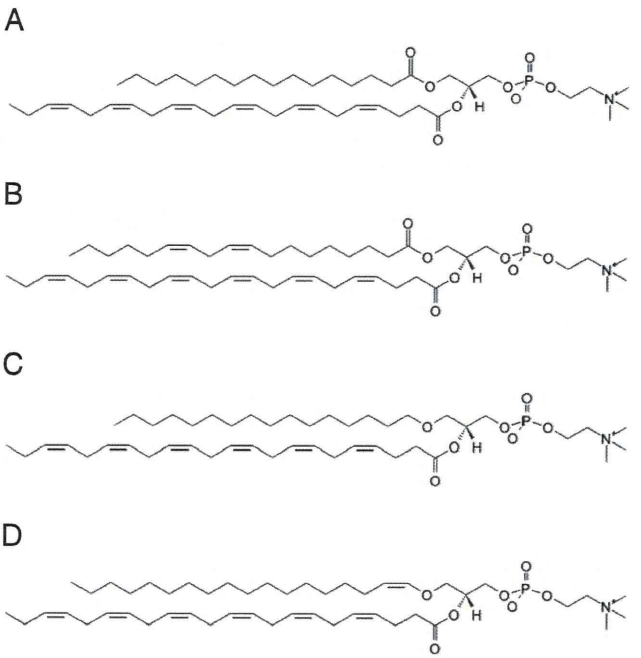

Fig. 7. Phosphatidylcholines that are seen in the control are structurally similar to HIGA-specific O-phosphatidylcholines. Determined or speculated primary structures of selected molecules are shown. Two common phosphatidylcholines that were seen in the cortex area, PC(16:0/22:6) (A) and PC(18:2/22:6) (B), are structurally similar to the HIGA-specific O-phosphatidylcholines, PC(O-16:0/22:6) (C) and PC(O-18:1/22:6), that are seen in the tubular areas and urine (D). The position of the double bonds in the side chains 18:2 and 18:1 were not determined, and therefore the most possible structures, PC(18:2/22:6) and PC(O-18:1/22:6), are shown.

Acknowledgment

We thank Koei Okazaki from Kazusa DNA Research Institute for performing the LC-LTQ-Orbitrap-MS analysis and Ms. Ryoko Yamamoto for excellent experimental assistance.

References

Baronas, E.T., Lee, J.W., Alden, C., Hsieh, F.Y., 2007. Biomarkers to monitor drug-induced phospholipidosis. Toxicol. Appl. Pharmacol. 218, 72–78.
Bligh, E.G., Dyer, W.J., 1959. A rapid method of total lipid extraction and purification. Can. J. Biochem. Physiol. 37, 911–917.
Coppo, R., Fonsato, V., Balegno, S., Ricotti, E., Loiacono, E., Camilla, R., Peruzzi, L., Amore, A., Bussolati, B., Camussi, G., 2010. Aberrantly glycosylated IgA1 induces mesangial cells to produce platelet-activating factor that mediates nephrin loss in cultured podocytes. Kidney Int. 77, 417–427.
Drummond, S.P., Allen, T.D., 2008. From live-cell imaging to scanning electron microscopy (SEM): the use of green fluorescent protein (GFP) as a common label. Methods Cell Biol. 88, 97–108.
Grunkin, M., Raundahl, J., Foged, N.T., 2011. Practical considerations of image analysis and quantification of signal transduction IHC staining. Methods Mol. Biol. 717, 143–154.
Hayasaka, T., Goto-Inoue, N., Sugiura, Y., Zaima, N., Nakanishi, H., Ohishi, K., Nakanishi, S., Naito, T., Taguchi, R., Setou, M., 2008. Matrix-assisted laser desorption/ionization quadrupole ion trap time-of-flight (MALDI-QIT-TOF)-based imaging mass spectrometry reveals a layered distribution of phospholipid molecular species in the mouse retina. Rapid Commun. Mass Spectrom. 22, 3415–3426.
Iijima, Y., Nakamura, Y., Ogata, Y., Tanaka, K., Sakurai, N., Suda, K., Suzuki, T., Suzuki, H., Okazaki, K., Kitayama, M., Kanaya, S., Aoki, K., Shibata, D., 2008. Metabolite annotations based on the integration of mass spectral information. Plant J. 54, 949–962.

Kurashige, T., Abe, K., Furusu, A., Miyazaki, M., Obata, Y., Xia, Z., Nakazawa, M., Nakazawa, Y., Funakoshi, S., Harada, T., Koji, T., Kohno, S., 2008. Renoprotective effect of azelnidipine in rats. Biol. Pharm. Bull. 31, 2237–2244.

Li, L., Zepeda-Orozco, D., Black, R., Lin, F., 2010. Autophagy is a component of epithelial cell fate in obstructive uropathy. Am. J. Pathol. 176, 1767–1778.

Mimura, K., Zhao, B., Muguruma, K., Frenkel, R.A., Johnston, J.M., 1996. Changes in glycerophospholipid profile in experimental nephrotic syndrome. Metabolism 45, 822–826.

Muda, A.O., Feriozzi, S., Rahimi, S., Faraggiana, T., 1995. Spatial arrangement of IgA and C3 as prognostic indicator of IgA nephropathy. J. Pathol. 177, 201–208.

Muso, E., Yoshida, H., Takeuchi, E., Yashiro, M., Matsushima, H., Oyama, A., Suyama, K., Kawamura, T., Kamata, T., Miyawaki, S., Izui, S., Sasayama, S., 1996. Enhanced production of glomerular extracellular matrix in a new mouse strain of high serum IgA ddY mice. Kidney Int. 50, 1946–1957.

Robinson, D.R., Tateno, S., Patel, B., Hirai, A., 1988. Dietary marine lipids after the course of autoimmune disease. Prog. Clin. Biol. Res. 282, 295–303.

Setou, M., Kurabe, N., 2011. Mass microscopy: high-resolution imaging mass spectrometry. J. Electron Microsc. (Tokyo) 60, 47–56.

Sugiura, Y., Setou, M., 2009. Selective imaging of positively charged polar and nonpolar lipids by optimizing matrix solution composition. Rapid Commun. Mass Spectrom. 23, 3269–3278.

Willems, S.M., van Remoortere, A., van Zeijl, R., Deelder, A.M., McDonnell, L.A., Hogendoorn, P.C., 2010. Imaging mass spectrometry of myxoid sarcomas identifies proteins and lipids specific to tumour type and grade, and reveals biochemical intratumour heterogeneity. J. Pathol. 222, 400–409.

Yasuda, Y., Cohen, C.D., Henger, A., Kretzler, M., 2006. The European Renal cDNA Bank (ERCB) Consortium: Gene expression profiling analysis in nephrology: towards molecular definition of renal disease. Clin. Exp. Nephrol. 10, 91–98.

Yoshioka, Y., Tsutsumi, T., Adachi, M., Tokumura, A., 2009. Altered phospholipid profile in urine of rats with unilateral ureteral obstruction. Metabolomics 5, 429–433.

Zhang, H., Saha, J., Byun, J., Schin, M., Lorenz, M., Kennedy, R.T., Kretzler, M., Feldman, E.L., Pennathur, S., Brosius III, F.C., 2008. Rosiglitazone reduces renal and plasma markers of oxidative injury and reverses urinary metabolite abnormalities in the amelioration of diabetic nephropathy. Am. J. Physiol. Renal Physiol. 295, F1071–F1081.

Anal Bioanal Chem (2011) 400:1895–1904
DOI 10.1007/s00216-011-4895-5

ORIGINAL PAPER

Semi-quantitative analyses of metabolic systems of human colon cancer metastatic xenografts in livers of superimmunodeficient NOG mice

Akiko Kubo · Mitsuyo Ohmura · Masatoshi Wakui · Takahiro Harada · Shigeki Kajihara · Kiyoshi Ogawa · Hiroshi Suemizu · Masato Nakamura · Mitsutoshi Setou · Makoto Suematsu

Received: 29 November 2010 / Revised: 7 February 2011 / Accepted: 9 March 2011 / Published online: 10 April 2011

Abstract Analyses of energy metabolism in human cancer have been difficult because of rapid turnover of the metabolites and difficulties in reducing time for collecting clinical samples under surgical procedures. Utilization of xenograft transplantation of human-derived colon cancer HCT116 cells in spleens of superimmunodeficient NOD/SCID/IL-2Rγ^{null} (NOG) mice led us to establish an experimental model of hepatic micrometastasis of the solid tumor, whereby analyses of the tissue sections collected by snap-frozen procedures through newly developed microscopic imaging mass spectrometry (MIMS) revealed distinct spatial distribution of a variety of metabolites. To perform intergroup comparison of the signal intensities of metabolites among different tissue sections collected from mice in fed states, we combined matrix-assisted laser desorption/ionization time-of-flight imaging mass spectrometry (MALDI–TOF-IMS) and capillary electrophoresis–mass spectrometry (CE–MS), to determine the apparent contents of individual metabolites in serial tissue sections. The results indicated significant elevation of ATP and energy charge in both

The first two authors equally contributed to this work.

Published in the special issue *Biomedical Mass Spectrometry* with Guest Editors Hisao Oka and Mitsutoshi Setou.

Electronic supplementary material The online version of this article (doi:10.1007/s00216-011-4895-5) contains supplementary material, which is available to authorized users.

A. Kubo · M. Ohmura · M. Suematsu
Department of Biochemistry, School of Medicine,
Keio University,
35 Shinanomachi, Shinjuku-ku,
Tokyo 160–8582, Japan

M. Ohmura · M. Suematsu (✉)
Japan Science and Technology Agency (JST),
Exploratory Research for Advanced Technology
(ERATO) Suematsu Gas Biology Project,
35 Shinanomachi, Shinjuku-ku,
Tokyo 160–8582, Japan
e-mail: msuem@sc.itc.keio.ac.jp

M. Wakui
Department of Laboratory Medicine,
School of Medicine,
Keio University,
35 Shinanomachi, Shinjuku-ku,
Tokyo 160–8582, Japan

T. Harada · S. Kajihara · K. Ogawa
Technology Research Laboratory, Shimadzu Corporation,
3-9-4 Hikaridai, Seika-cho, Soraku-gun,
Kyoto 619–0237, Japan

H. Suemizu · M. Nakamura
Central Institute for Experimental Animals,
1430 Nogawa, Miyamae-ku, Kawasaki-shi,
Kanagawa 216–0001, Japan

M. Nakamura
Department of Pathology and Regenerative Medicine,
Tokai University School of Medicine,
143 Shimokasuya, Isehara-shi,
Kanagawa 259–1193, Japan

M. Setou
Department of Molecular Anatomy,
Molecular Imaging Frontier Research Center,
Hamamatsu University School of Medicine,
1-20-1 Handayama, Higashi-ku, Hamamatsu-shi,
Shizuoka 431–3192, Japan

metastases and the parenchyma of the tumor-bearing livers. To note were significant increases in UDP-*N*-acetyl hexosamines, and reduced and oxidized forms of glutathione in the metastatic foci versus the liver parenchyma. These findings thus provided a potentially important method for characterizing the properties of metabolic systems of human-derived cancer and the host tissues in vivo.

Keywords Imaging mass spectrometry (IMS) · Matrix-assisted laser desorption/ionization (MALDI) · Capillary electrophoresis–mass spectrometry (CE–MS) · Tumor-bearing liver · Metabolome · Glycoprotein biosynthesis

Abbreviations

CE–MS	capillary electrophoresis–mass spectrometry
MALDI	matrix assisted laser desorption/ionization

Introduction

Imaging mass spectrometry (IMS) has enabled us to collect spatial information about a variety of biomolecules, for example phospholipids [1, 2], drugs [3], peptides [4, 5], and metabolites [6–8] in tissue sections in situ. Many kinds of ion sources for imaging mass spectrometry had been developed in recent years. For example, ultraviolet matrix-assisted laser desorption/ionization (MALDI) is capable of producing ions from low-molecular-mass compounds, being promising for imaging volatile compounds in fresh ginger samples [9]. Low-molecular-mass metabolites have also been analyzed by other methods including desorption electrospray ionization and desorption/ionization on silicon [10, 11]. In these methods, samples should be dried before image acquisition of metabolomic snapshots to avoid enzymatic degradation of the molecule of interest. On the other hand, laser ablation electrospray ionization or infrared MALDI are other useful methods of molecular imaging that are applicable to water-rich specimens to ionize the analytes [12, 13].

In order to acquire reliable images of metabolites in and around cancers in vivo, several lines of methodological consideration are necessary. First, enzymatic reactions in tissue and cell samples should be terminated as soon as possible. Second, soft ionization of the molecules seemed desirable to identify individual peaks of metabolites. Finally, high spatial resolution at cellular levels is required to examine differences in metabolic properties between the cancer foci and the surrounding host tissues. In this context, application of ultraviolet MALDI to freeze-dried tissue samples is suitable for examining cancer metabolism in vivo. Regarding the spatial resolution of the ultraviolet MALDI, the raster scan pitch of the laser application has been restricted by its focusing diameter, in the approximate range 50–200 μm [7, 8]. Our newly developed UV–MALDI–quadrupole ion-trap (QIT)-TOF-MS instrument, that is, a mass microscope with 10-μm spatial resolution, overcame this problem of spatial resolution by improvement of the ion source to control the position of the sample stage three-dimensionally with high accuracy [9, 14, 15]. Using 9-aminoacridine as a matrix, metabolites, such as high-energy nucleotides and phosphorylated carbohydrates became directly detectable in frozen tissue sections [6]. Since then, various types of tissues including brain and muscles of mice have been analyzed experimentally to dissect molecular mechanisms for metabolic systems in vivo [7, 8, 16].

The objective of this study was to characterize metabolic systems in and around human-derived solid tumors in vivo. Although distinct properties of cancer metabolism known as Warburg effects have been examined mainly in cultured systems or conventional animal experiments, there are several technical difficulties in characterizing the metabolism of human solid tumors in vivo. First, it is difficult to shorten the time for sampling of tissues to avoid degradation of metabolites with rapid turnover under surgical procedures. Second, because of large variances of the mass intensities of molecules among individual tissue samples, a method to semi-quantify their signals and to compare these among individual samples should be developed. To overcome the first problem, we have herein utilized an experimental model of xenograft transplantation of human-derived colon cancer HCT 116 cell line in superimmunodeficient NOD/SCID/IL-2Rγ^{null} (NOG) mice [17]. In this model, we were able to collect snap-frozen samples of the tumor-bearing liver for analyses by using imaging mass spectrometry with high spatial resolution. To solve the second problem, we used serial sections of the liver to determine total amounts of individual metabolites, using CE–MS for data calibration. This method enabled us to carry out intergroup comparison of semi-quantitative metabolite data in and around micrometastases of the human-derived colon cancer. Results obtained in this study revealed that the tumor-bearing liver accelerates its energy metabolism. Furthermore, several metabolites including UDP-*N*-acetyl hexosamine (UDP-HexNAc) and glutathione, and the value of energy charge were significantly elevated in the metastatic foci, suggesting significance of these molecules as marker metabolites enriched in the cancer in vivo.

Experimental

Chemicals

9-Aminoacridine (9-AA) was purchased from Merck Schuchardt (Hohenbrunn, Germany). All chemical stan-

dards were obtained from common commercial sources and dissolved in Milli-Q (Millipore) water, 0.1 mol L^{-1} HCl, or 0.1 mol L^{-1} NaOH to furnish 10 mmol L^{-1} or 100 mmol L^{-1} stock solutions. Distilled water purified by use of a Milli-Q water system was used for all the preparations. Working standard mixtures were prepared by diluting stock solutions with Milli-Q water immediately before injection of samples for CE–MS analysis. The chemicals used were analytical or reagent grades.

Animal model to observe growth of human-derived cancer in vivo

Care and use of laboratory animals were in accordance with the Experimental Animal Committee of Keio University School of Medicine which followed the Guidelines for the Proper Conduct of Animal Experiments by the Science Council of Japan. We herein applied an experimental model using superimmunodeficient NOD/SCID/IL-2Rγ^{null} (NOG) mice [18] which lack T-cells, B-cells, and NK cells, enabling xenograft transplantation of the human-derived colon cancer cell line HCT116 transfected with *venus*, a GFP-mutant gene (HCT116/*venus*) was injected intrasplenically as described elsewhere [17, 19]. To our knowledge, the system using NOG mice serves as a reliable experimental model in which human-derived cancer cell lines transplanted in vivo generate metastases forming solid tumors in organs including the liver in vivo with greater reproducibility than the conventional model using NOD mice which lack T-cells and B-cells but not NK cells [17]. In the intrasplenic implantation model using HCT116/*venus*, micrometastases of the cancer occurred mostly in periportal regions of the liver within one week, extending their size over the following three weeks [19]. In this study, male mice at 11–13 weeks were fed with Laboratory chow and allowed free access to water. They were anesthetized by use of pentobarbital sodium, and their abdominal walls were cut to exteriorize the portion of the liver lobules for snap-frozen procedures using liquid nitrogen as described elsewhere [20, 21]. The livers of the xenograft-transplanted NOG mice used for the analyses were collected under fed conditions two weeks after the xenograft transplantation, unless otherwise mentioned.

Tissue preparation

A schematic diagram of a standard experimental design typical of tissue section application can be seen in the Electronic Supplementary Material (Fig. S1). The liver tissues snap-frozen in liquid nitrogen were dissected to prepare cryosections with 5-μm thickness by use of a cryostat (CM 1900; Leica Microsystems, Wetzlar, Germany). The sections were thaw-mounted on indium–tin oxide (ITO) slides (8–12 ohm/sq; Sigma, Chiba, Japan) and were dried in silica gel-containing plastic tubes then sprayed with 9-aminoacridine (9-AA, 20 mg in 4 mL 70% MeOH) by use of a 0.2-mm nozzle caliber airbrush (Procon boy FWA Platinum; Mr Hobby, Tokyo, Japan) to conduct MALDI–IMS in negative ion mode. Adjacent sections were fixed with 10% buffered formalin (Nacalai Tesque, Kyoto, Japan) and stained with the Masson trichrome staining reagent kit according to the manufacturer's procedures (Muto Pure Chemicals, Tokyo, Japan). The other frozen tissues were used for metabolome analyses using CE–MS.

Instruments

An atmospheric pressure MALDI–QIT-TOF-MS equipped with a 355-nm Nd:YAG laser and a built-in fluorescence microscope furnished mass images with high spatial resolution of 10 μm, as described for a prototype IMS machine [9] (Mass Microscope; Shimadzu, Kyoto, Japan). The microscope was also equipped with a 120-W metal halide light source (X-Cite 120PC-Q; Lumen Dynamics Group, Ontario, Canada) and a fluorescence mirror unit (U-MGFPHQ; Olympus, Tokyo, Japan) that enabled us to visualize *venus*-associated green fluorescence from metastatic foci in tissue slices before matrix application. This system thus enabled us to collect both fluorescence images and mass images from the same tissue slices. Before applying matrices, a fluorescence image of the analyte was acquired and followed by recording the location of the specimen on the *XYZ* stage. ITO slides with the sample holder were removed from the *XYZ* stage, and sprayed uniformly with 4 mL 9-AA solution. After application of the matrix, the sample holder was placed back on the *XYZ* stage, which was adjusted to exactly the same location. The mass spectra of the designated areas on a specimen photographed before matrix application were acquired in the negative-ion mode. The data collected through the microscopic system were digitally processed according to the method described later, in the section "*Determination of the apparent contents of metabolites based on data calibration by CE–MS*". Experiments using capillary electrophoresis electrospray ionization mass spectrometry (CE–MS) were performed with a capillary electrophoresis system equipped with an air pressure pump, MSD quadrupole MS, isocratic HPLC pump, and CE–MS adapter kit (Agilent Technologies, Waldbronn, Germany) [20, 22]. All system control, data acquisition, and MSD data evaluation were performed using Agilent G2201A ChemStation software for CE–MSD.

Conditions for MALDI imaging and tandem MS analyses

All the MALDI imaging experiments and tandem MS experiments were carried out in negative-ion mode using a prototype mass microscope. The laser power was adjusted

to the desired intensities. MALDI mass spectra were acquired under the conditions laser frequency 800 Hz and scanning mass range from *m/z* 260 to *m/z* 900. Regions of the tissue samples exposed to the laser irradiation were determined by light and fluorescence microscopic observations. A raster scan on the tissue surface was performed automatically (250×250 spots per scan). Laser irradiation was repeated 160 times for the individual spots. The spatial interval of data points was 10 μm, giving 62,500 data points in total for each section. Tandem MS analyses were performed to determine the structures of metabolites at appropriate laser energy, argon gas percentage, and collision-induced dissociation (CID) energy conditions. To identify metabolites detected in MALDI–IMS, we searched the Human Metabolome Database (http://hmdb.ca) and performed tandem MS analyses, comparing the tandem mass spectra with those from standard reagents using 9-AA as the matrix of choice in negative mode. The distribution of biomolecules that were identifies by MS^2 analysis were visualized as mass images using BioMap software (http://www.maldi-msi.org) from Novartis (Basel, Switzerland).

Determination of the apparent contents of metabolites based on data calibration by CE–MS

To compare differences in contents of many different metabolites in multiple tissue slices collected from different subjects, we conducted CE–MS-based metabolome analyses of tissue lysates collected from the same snap-frozen liver samples for IMS. As reported previously [20–22], CE–MS enabled us to quantitatively determine more than 2,000 different metabolites at once in small amounts of a single liver sample. Small amounts of the frozen tissue were collected from thick section that was adjacent to the section for IMS. The CE–MS samples weighing approximately 300 mg wet weight was ground using a multi-bead shocker (model MB755U; Yasui Kikai, Osaka, Japan) with frozen metal granules, and 1 mL methanol containing internal standards (300 μmol L^{-1} each of L-methionine sulfone and 2-morpholinoethanesulfonic acid (MES)) was added. After addition of 0.5 mL deionized water and 1 mL chloroform, the mixture was centrifuged at 15,000 rpm for 15 min at 4 °C. The upper aqueous layer of the sample was filtered through the 5-kDa cutoff filter (Millipore, Tokyo, Japan) by centrifugation to remove protein components. The filtrate was lyophilized and dissolved in 200 μL deionized water containing reference compounds (200 μmol L^{-1} each of 3-aminopyrrolidine and trimesate). The amounts of metabolites were normalized by liver weight of the original tissue samples. Assuming that 1 mg wet tissue was equivalent to 1 μL, apparent contents of individual metabolites were calculated for the data calibration in imaging mass microscopy by computer-assisted data processing in the later session.

To semi-quantify apparent contents of individual metabolites mapped on the images, regions of interest (ROIs) for the cancer xenografts and the liver parenchyma were selected by careful visual inspection of fluorescence and light microscopic images. Averaged spectra from each ROI were generated and statistically analyzed by use of the laboratory-written software SIMtools (Shimadzu Imaging Mass spectrometry toolbox for MATLAB). The Mann–Whitney U-test was used to compare the ion signal intensity between the tumor and the liver parenchyma.

To calculate apparent contents of metabolites in IMS, mass signals covering *m/z* between 260 and 620 were collected from 250×250 spots on a tissue sample. Direct comparison of metabolite ion signals among different slices requires realistic transformation of acquired mass signals of a metabolite in absolute terms, for example tissue contents in nmol g^{-1} tissue. To that effect, apparent contents of a specific metabolite in the ROI designated as liver parenchyma ($[C_{\mathrm{Liver}}]_{\mathrm{app}}$) or tumor ($[C_{\mathrm{Tumor}}]_{\mathrm{app}}$) were calculated by use of Eqs. 1, 2, and 3:

$$[C_{\mathrm{Tumor}}]_{\mathrm{app}} = [C_{\mathrm{Average}}] \times (I_{\mathrm{Tumor}}/I_{\mathrm{Average}}) \quad (1)$$

$$[C_{\mathrm{Liver}}]_{\mathrm{app}} = [C_{\mathrm{Average}}] \times (I_{\mathrm{Liver}}/I_{\mathrm{Average}}) \quad (2)$$

$$I_{\mathrm{Average}} = (I_{\mathrm{Liver}} \times O_{\mathrm{Liver}})/100 + (I_{\mathrm{Tumor}} \times O_{\mathrm{Tumor}})/100 \quad (3)$$

where $[C_{\mathrm{Average}}]$ denotes the amount of a metabolite of interest in the whole tissue section for IMS (nmol g^{-1} tissue). I_{Tumor}, I_{Liver}, and I_{Average} are MALDI signal intensities measured in regions of tumor metastases, liver parenchyma, and the whole tissue section, respectively. O_{Tumor} and O_{Liver} are the percentage areas of tumor regions and liver parenchyma, respectively, in tumor-bearing livers. These indices were designated by the green fluorescence intensities acquired by fluorescence microscopy of the whole frozen section using Image J software (NIH, http://rsbweb.nih.gov/ij/index.html). Assuming that percentages of tumor-bearing regions in the tissue sections are comparable with those of the metastases in the adjacent tissue samples for the CE–MS measurements, the values of $[C_{\mathrm{Average}}]$ can be replaced by $[C_{\mathrm{CE-MS}}]$, the amounts of the metabolites of interest in the tissue samples for CE–MS, as seen in Eqs. 1′ and 2′.

$$[C_{\mathrm{Tumor}}]_{\mathrm{app}} = [C_{\mathrm{CE-MS}}] \times (I_{\mathrm{Tumor}}/I_{\mathrm{Average}}) \quad (1')$$

$$[C_{\mathrm{Liver}}]_{\mathrm{app}} = [C_{\mathrm{CE-MS}}] \times (I_{\mathrm{Liver}}/I_{\mathrm{Average}}) \quad (2')$$

In order to calculate the values for $[C_{\mathrm{Tumor}}]_{\mathrm{app}}$ and $[C_{\mathrm{Liver}}]_{\mathrm{app}}$, I_{Tumor}, I_{Liver}, and I_{Average} were determined in

three different ROIs in a single tissue specimen, while the corresponding value of $[C_{CE-MS}]$ was collected from a portion of the tissue adjacent to the samples for IMS. A set of mass-imaging data paired with CE–MS data in a single animal were repeated for four separate animals.

To construct an ion-content map, data collected by MALDI–QIT-MS were saved and digitally processed to be converted to Analyze format, a common multidimensional biomedical imaging format file. The Analyze format file was processed to construct an ion-content map, where the relationship between the apparent content of a metabolite of interest at a pixel "i" (Ci) and the MALDI signal intensity in the same pixel ($I_{(i)}$) was expressed by Eq. 4:

$$Ci = [C_{CE-MS}] \times \left(I_{(i)}/I_{Average}\right) \quad (4)$$

Validation of the calibrated data in IMS by analysis of high-energy adenylates in vivo

Reliability of the calibrated data seemed to depend on multiple factors including the quality of CE–MS-based metabolome analysis and that of tissue-sampling procedures in the snap-frozen processes. In accordance with our previous studies [7], we determined apparent contents of ATP, ADP, and AMP by IMS combined with CE–MS. Based on these data, apparent energy charge of individual pixels were calculated by use of Eq. 5:

$$\text{Apparent energy charge } (EC_{app}) = \left([ATP]_{app} + 1/2[ADP]_{app}\right)/\left([ATP]_{app} + [ADP]_{app} + [AMP]_{app}\right) \quad (5)$$

Statistics

Differences between mean values for two groups were statistically analyzed by use of the Mann–Whitney U-test. $P<0.05$ was considered statistically significant.

Results and discussion

Detection of metabolites from normal mouse liver tissue

As shown in Fig. 1, MALDI–MS analyses in the negative-ion mode using 9-AA as the matrix revealed the presence of many signals including nucleotides on the liver tissue frozen section with minimal interference from the matrix, as reported by Edwards and Kennedy [6]. Among these peaks, 16 intense mass peaks were assigned using their exact masses to nucleotides, nucleotide-sugar conjugates, 2,3-bisphosphoglycerate (2,3-BPG), taurocholate, and both reduced and oxidized forms of glutathione. Assignment of these metabolites was verified by structural analysis of individual peaks using tandem MS. In the region adjacent to those for mass-imaging experiments in the same section, the peaks generated on the tissue surface were identified by fragmentation using MALDI–QIT-TOF MS [9]. Table 1 summarizes the results of MS and MS^2 analyses. Among the individual mass peaks of nucleoside-monophosphate, the ribose-phosphate structure was present (211.0 fragment ions and neutral losses of adenine, uridine, and guanidine from precursor ions respectively). Among the peaks of nucleotide–sugar conjugates, fragment ions derived from the UDP structure were confirmed (403.0 fragment ions and

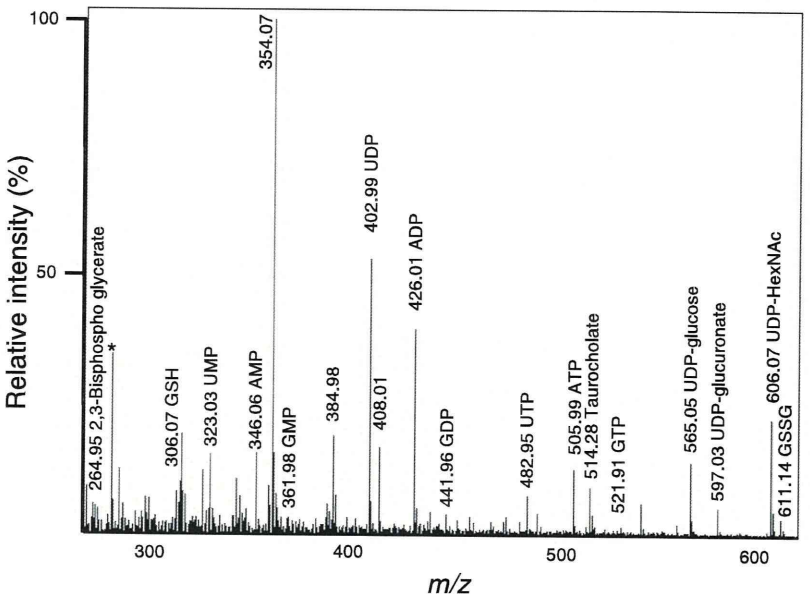

Fig. 1 Typical MALDI mass spectrum of the mouse liver collected from the "mass microscope" a MALDI–IT-TOF analyzer in the negative-ion mode. The signals ranging from m/z=260 to 620 were collected. Mass spectra of metabolites were obtained by integrating 10,000,000 consecutive laser shots (160 shots per subspectrum and 62,500 subspectra). Peaks identified in this study are labeled; that originating from the 9-AA matrix is indicated by an *asterisk*

Table 1 List of metabolites identified in the study, with their respective deprotonated *m/z* values and MS^2 ion species in the negative mode

No.	$[M-H]^-$ (*m/z*)	Fragments observed in MS^2	Formula	Identified
1	264.95	246.973, 179.043, 166.955	$C_3H_8O_{10}P_2$	2,3-Bisphosphoglycerate
2	306.07	254.087, 179.050, 143.048, 158.932, 210.092, 288.858, 120.041	$C_{10}H_{17}N_3O_6S$	Glutathione (GSH)
3	323.02	211.006, 280.028, 138.983, 158.922	$C_9H_{13}N_2O_9P$	UMP
4	403.00	304.984, 158.907, 384.935, 322.989, 290.931, 272.920	$C_9H_{14}N_2O_{12}P_2$	UDP
5	482.93	384.927, 272.919, 176.913, 158.905	$C_9H_{15}N_2O_{15}P_3$	UTP
6	346.05	211.000, 150.985, 134.049, 194.051	$C_{10}H_{14}N_5O_7P$	AMP
7	426.02	328.044, 134.053, 407.999, 329.037, 272.950, 290.945	$C_{10}H_{15}N_5O_{10}P_2$	ADP
8	505.98	408.022, 272.958, 158.922, 176.933, 392.003	$C_{10}H_{16}N_5O_{13}P_3$	ATP
9	361.98	210.985, 260.838, 158.908	$C_{10}H_{14}N_5O_8P$	GMP
10	441.96	343.992, 150.025, 158.909	$C_{10}H_{15}N_5O_{11}P_2$	GDP
11	521.91	423.940, 272.924, 176.911, 158.906, 229.979	$C_{10}H_{16}N_5O_{14}P_3$	GTP
12	565.03	323.024, 306.072, 402.984, 211.000, 384.977	$C_{15}H_{24}N_2O_{17}P_2$	UDP-glucose (UDP-Hexose)
13	579.02	323.027, 402.997, 254.996, 305.011, 210.994	$C_{15}H_{22}N_2O_{18}P_2$	UDP-glucuronic acid
14	606.06	384.9445, 402.996, 282.045, 272.956, 323.038, 305.017, 362.008	$C_{17}H_{27}N_3O_{17}P_2$	UDP-GlcNAc (UDP-HexNAc)
15	611.14	306.071, 272.086, 338.058, 254.079, 482.103, 304.058, 288.058, 593.121	$C_{20}H_{32}N_6O_{12}S_2$	Glutathione, oxidized (GSSG)

neutral loss of each hexose, glucuronic acid, and *N*-acetylhexosamines). All the assigned and verified metabolites in Table 1 were compared with commercial standard compounds under appropriate MALDI and CID tandem MS conditions.

Intralobular distributions of metabolites in the liver

Figure 2 shows the tissue distribution of metabolites in the control fed liver of NOG mice. As seen in Figs. 2a and b, by use of Masson trichrome staining we were able to distinguish portal and central venules by judging the presence of bile ducts as a typical structure of the portal triad. Worthy of note is that the intraluminal space of the portal (P) and central venules indicated strong signals of 2,3-BPG (Fig. 2d) whereas taurocholate, the taurine-conjugated form of cholic acid, was evident in bile ducts (B) adjacent to the portal venules and periportal parenchyma, showing a typical P–P bridging pattern (Fig. 2e). On the other hand, UDP-glucuronate, a substrate for glucuronidization of xenobiotic compounds was localized mainly in pericentral regions, with a pattern distinct from that of taurocholate (Fig. 2f). Such an intralobular microanatomical relationship among periportal and pericentral regions and the microvessels was well demonstrated by superimposition of taurocholate (*m/z* 514.28; green in Figs. 2g and h) with 2,3-BPG (*m/z* 264.95; red in Fig. 2g) or UDP-glucuronate (*m/z* 579.03; red in Fig. 2h), respectively. In contrast, an intralobular pattern of UDP-HexNAc was distinct, distributing homogeneously over the whole liver parenchyma (Fig. 2i). These results suggest that several different metabolites such as 2,3-BPG, taurocholate, and UDP-glucuronate visualized by use of this method serve as reliable markers to distinguish vascular structures and periportal and pericentral regions in hepatic zonation. Such results were also consistent with previous observations as follows. First, 2,3-BPG occurs abundantly in red blood cells, being at approximately 5 mmol L^{-1} [23]. Secondly, taurocholate is synthesized and excreted to bile canaliculi around periportal hepatocytes [24, 25], whereas UDP-glucuronate is biosynthesized predominantly in pericentral hepatocytes, which had a large capacity for xenobiotic detoxification [26, 27]. Our approach to analysis of metabolites at the microscopic level, serves as a powerful tool to investigate intralobular heterogeneity in metabolic systems in the liver.

Distinct properties of energy metabolism between cancer metastases and liver parenchyma

Figure 3 shows representative pictures of high-energy adenylate phosphates in liver bearing colon cancer metastases under fed conditions. As seen in Figs. 3a and b, the micrometastases were clearly identified by green fluorescence generated by *venus*-expressing HCT116 cells. Figure 3c depicts mapping of apparent energy charge that was calculated from images of AMP, ADP, and ATP (Figs. 3d, e, and f, respectively). Worthy of note was that intralobular distribution of these three adenylates appeared almost homogeneous, whereas the energy charge composed from these images had a heterogeneous pattern, being greater at the sites of cancer metastasis than in the liver

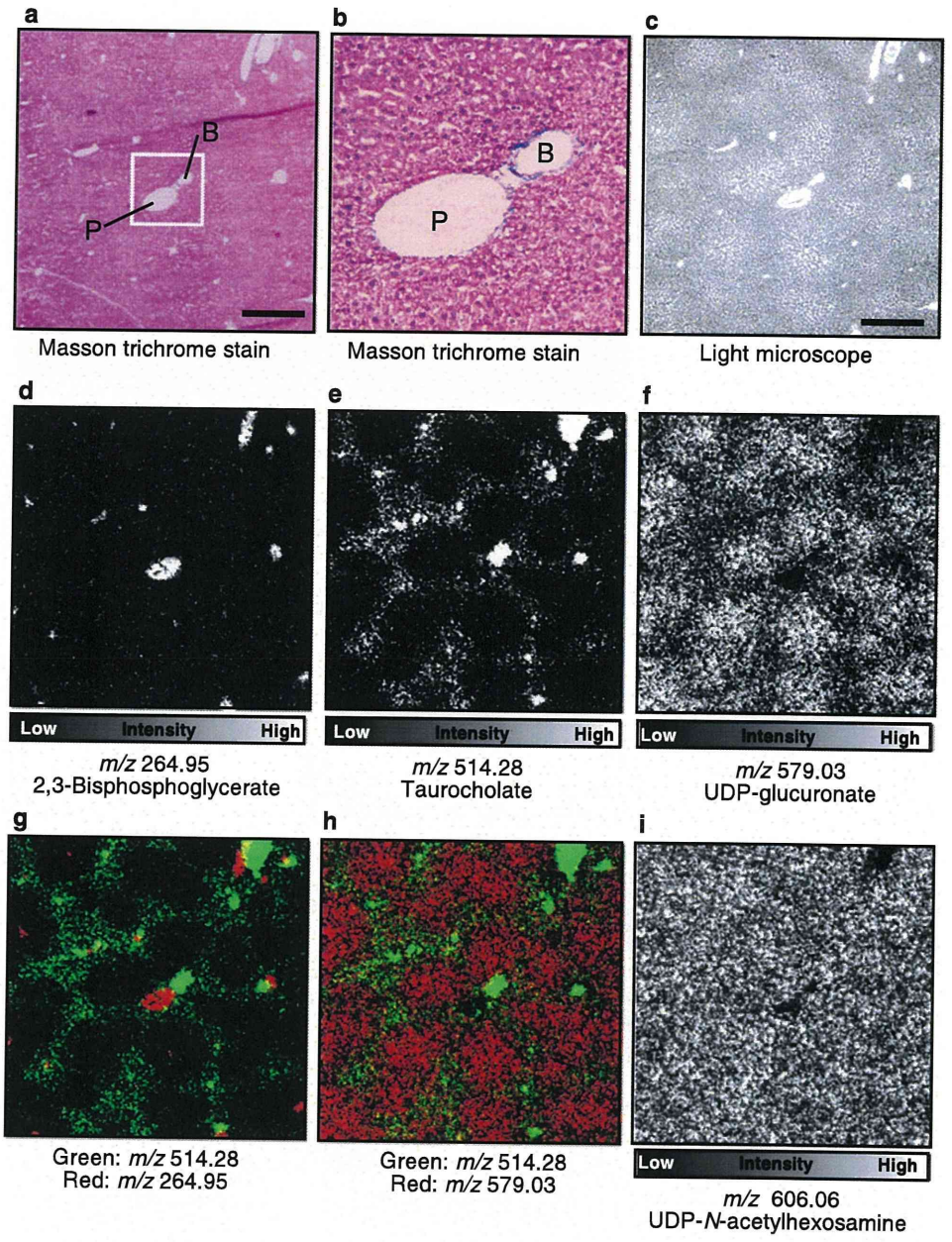

Fig. 2 In situ mass spectrometric imaging of metabolites in the control liver of an NOG mouse. **a** An optical image of a section stained with Masson's trichrome solutions. The stained section was adjacent to that was used for IMS. *Scale bar*: 500 μm, *B*:bile duct, *P*:portal venule. **b** the image with greater magnification of the area indicated by the *white square* in **a**. Collagen fibers in the portal triad were stained in blue. *B*:bile duct, *P*:portal venule. **c** Light-microscopic image of frozen liver section used in mass spectrometric imaging that was captured before matrix application. *Scale bar*: 500 μm. **d** An ion image of 2,3-bisphosphoglycerate (2,3-BPG) at m/z=264.95 and **e** taurocholate at m/z=514.28, **f** UDP-glucuronate at m/z=579.03. **g** The overlaid image of 2,3-BPG (*red*) and taurocholate (*green*). **h** UDP-glucuronate (*red*) and taurocholate (*green*). **i** UDP-HexNAc at m/z=606.06. A representative set of pictures from four separate experiments

parenchyma. So far as judged from the intensities, the apparent energy charge in the metastatic foci was approximately 0.8, while that in the parenchyma was 0.5–0.7, suggesting that the foci accelerate generation of high-energy adenylate phosphates. Of importance were semi-quantitative values of $[ATP]_{app}$ in the tumor-bearing liver (Fig. 3f), in the range of approximately 1–2 μmol g^{-1} liver, levels reasonably comparable with previous observations that determined absolute ATP contents under the snap-frozen procedures [20, 21]. Because intracellular levels of ATP are in the mmol L^{-1} range, current procedures for data calibration seemed to reproduce reliable intracellular concentrations of metabolites with a rapid turnover.

Glutathione and UDP-HexNAc serve as marker metabolites enriched in the cancer xenografts

Figure 4 shows representative pictures of UDP-HexNAc, reduced (GSH), and oxidized (GSSG) forms of glutathione. As seen in Figs. 4a–c, UDP-HexNAc was predominantly high in the tumor metastases. GSH and GSSG signals were also greater in the metastatic foci, but with a different pattern from that of UDP-HexNAc (Figs. 4d–f). When focusing on individual foci, UDP-HexNAc and GSH seemed to be demarcated from each other, suggesting these molecules occur in a spatially heterogeneous manner in an individual metastatic focus.

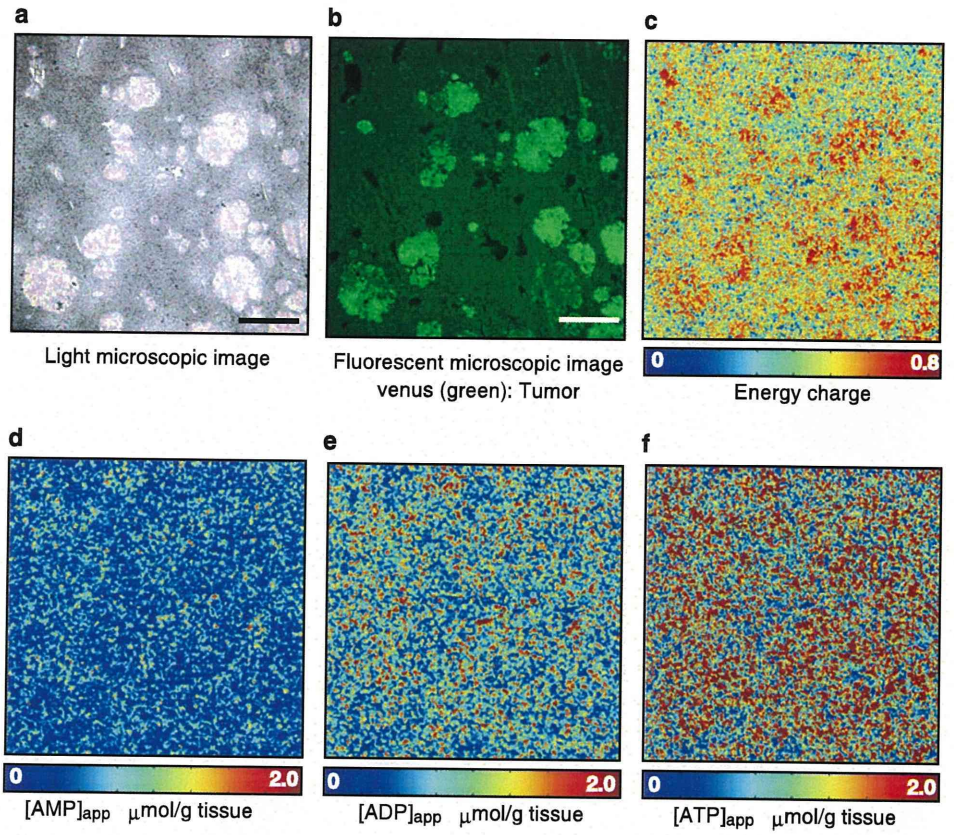

Fig. 3 Representative pictures indicating high-energy adenylate phosphates and apparent energy charge in the tumor-bearing livers of NOG mice. **a** A light-microscopic photograph of intrasplenically injected HCT116 colon cancer cell xenografts. *Scale bar*: 500 μm. **b** A green fluorescence image of the same region shown in (**a**). *Scale bar*: 500 μm. **c** A heat map of apparent energy charge calculated from apparent contents of tumor bearing-liver. **d–f** Heat maps of $[AMP]_{app}$, $[ADP]_{app}$, and $[ATP]_{app}$, respectively. A representative set of pictures from four separate experiments

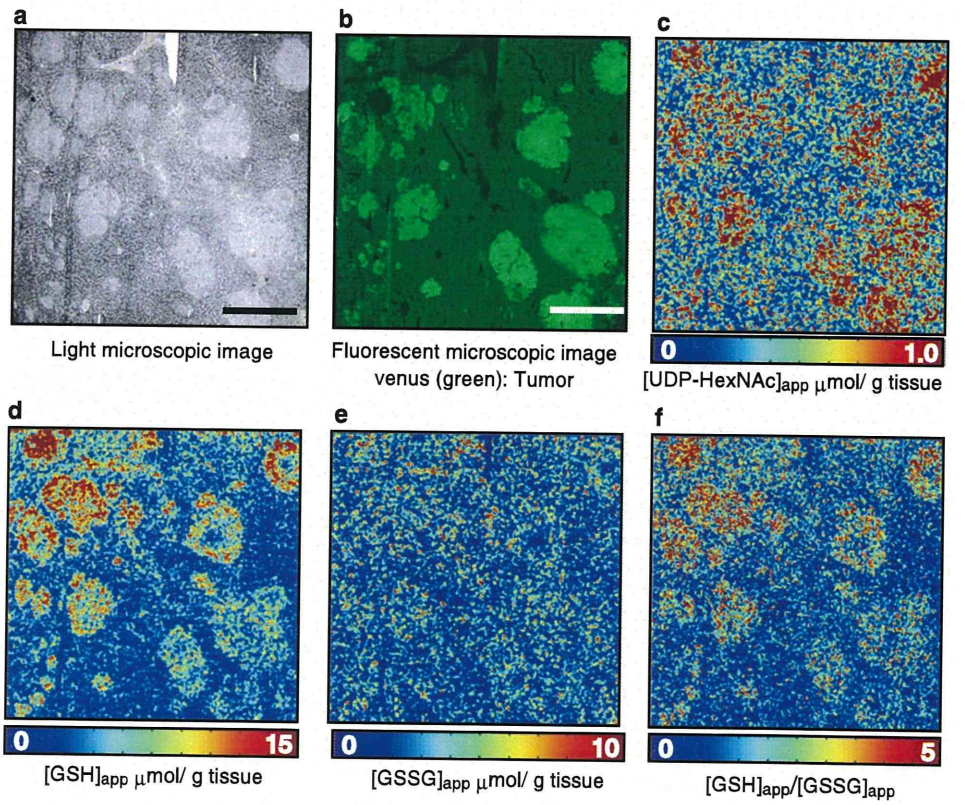

Fig. 4 Glutathione and UDP-HexNAc as marker metabolites enriched in hepatic cancer metastasis. **a** Light-microscopic photograph of intrasplenically injected HCT116 colon cancer cell xenografts in the liver of NOG mice. *Scale bar*: 500 μm. **b** A green fluorescence image of the same specimen shown in (**a**). *Scale bar*: 500 μm. **c** An apparent contents map of UDP-HexNAc at *m/z* 606.06. **d**, **e** Apparent contents maps of the reduced type of glutathione (GSH) at *m/z* 306.07, and oxidized glutathione (GSSG) at *m/z* 611.14. **f** $[GSH]_{app}/[GSSG]_{app}$ ratio imaging in the same microscopic field plotted as a heat map. A representative set of pictures from four separate experiments

Figure 5 illustrates semiquantitative comparison of these metabolites among different groups. As seen in Fig. 5a showing data collected from CE–MS, amounts of UDP-HexNAc in the tumor-bearing liver (tumor plus liver) were significantly greater than those in the control liver. On the other hand, amounts of GSH and GSSG were not significantly different between the groups. When MALDI–MS intensity ratios in IMS for these metabolites were analyzed (Fig. 5b), UDP-HexNAc, GSH, and GSSG were significantly elevated in the metastatic foci compared with those measured in the hepatic parenchyma. Such a trend was reproducible in the calibrated data showing apparent contents of these metabolites (Fig. 5c), suggesting that both forms of glutathione occurred prominently in the metastatic foci to greater extents than in the host liver parenchyma.

In the control liver, UDP-HexNAc which is an important substrate for polysaccharide chains including hyaluronic acid, was homogeneously distributed over the liver (Fig. 2i). As seen in Fig. 4, on the other hand, the colon cancer xenografts exhibited greater accumulation than the liver parenchyma. Ishimoto et al. and our laboratory have recently provided evidence that CD44, the hyaluronic acid receptor expressed on cancer stem cells, is responsible for stabilization of the cystine transporter xCT that accelerates uptake of cysteine and glutathione to increase their anti-oxidative capacity against cell death [28]. Because GSH detoxifies electrophiles through their conjugation by glutathione *S*-transferases, such accumulation of the thiol might contribute to survival of the cancer cells against anti-cancer reagents [29, 30]. Up to now, it remains still difficult to visualize amino acids globally by MALDI–MS with high spatial resolution. Improvement of the spatial resolution in the current IMS system together with development of the method to visualize amino acid metabolism deserves further studies provided that resources and mechanisms for delivery of amino acids to maintain GSH in cancer cells are revealed.

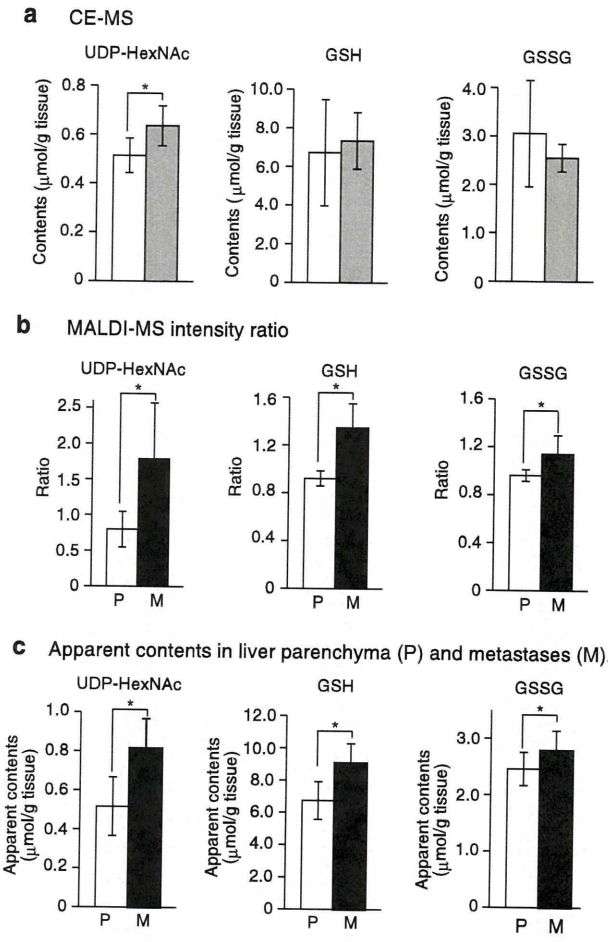

Fig. 5 Differences in contents of UDP-HexNAc, and reduced (*GSH*) and oxidized (*GSSG*) glutathione in the tumor-bearing-NOG liver. **a** Differences in CE–MS data between the control (*open columns*) and the tumor-bearing livers (*dark columns*) of NOG mice. **b** The MALDI–MS signal intensity ratio of UDP-HexNAc, GSH, and GSSG in the parenchyma (*P; open columns*) and metastatic foci (*M; closed columns*) versus the average MALDI–MS intensity of the ROIs as a whole. *Bars* indicate SD. **P*<0.05 according to Mann–Whitney *U*-tests. **c** Apparent amounts of UDP-HexNAc, GSH, and GSSG in the parenchyma (*P; open columns*) and metastatic foci (*M; closed columns*). *Bars* indicate SD from four separate experiments. **P*<0.05, Mann–Whitney *U*-tests

Conclusion

Comparison of differences in metabolomic profiles between control livers and those bearing metastatic foci of the human colon cancer enabled us to reveal distinct metabolic features between the two regions. IMS using 9-aminoacridine enabled us to detect nucleotides, lipids, and several aminosugars. The metastatic human colon cancer xenografts displayed remarkable accumulation of UDP-HexNAc and glutathione in vivo, serving as marker metabolites. Newly developed IMS combined with CE–MS measurements serves as a potentially reliable method to perform intergroup comparison of varied metabolites among different tissue specimens. Future investigation is necessary to establish methodology for use of the current technique in diagnostic medicine.

Acknowledgements The authors are grateful to Masaaki Matsuura (Japan Federation of Cancer Research) and all the member of the SENTAN project (Shimadzu Corporation), Kenji Kawai (Central Institute for Experimental Animals), and members of Suematsu Laboratory for providing considerable support for our research. The authors acknowledge support for this work by a Grant-in-Aid for SENTAN from the Japan Science and Technology Agency (to M.Se. and M.W) and from the JST ERATO Suematsu Gas Biology Project (to M.Su). Design of CE–MS-based metabolome analysis in this study was supported by Research and Development of the Next-Generation Integrated Simulation of Living Matter, a part of the Development and Use of the Next-Generation Supercomputer Project of MEXT.

References

1. Sugiura Y, Konishi Y, Zaima N, Kajihara S, Nakanishi H, Taguchi R, Setou M (2009) Visualization of the cell-selective distribution of PUFA-containing phosphatidylcholines in mouse brain by imaging mass spectrometry. J Lipid Res 50:1776–1788
2. Shimma S, Sugiura Y, Hayasaka T, Zaima N, Matsumoto M, Setou M (2008) Mass imaging and identification of biomolecules with MALDI–QIT-TOF-based system. Anal Chem 80:878–885
3. Khatib-Shahidi S, Andersson M, Herman JL, Gillespie TA, Caprioli RM (2006) Direct molecular analysis of whole-body animal tissue sections by imaging MALDI mass spectrometry. Anal Chem 78:6448–6456
4. Stoeckli M, Chaurand P, Hallahan DE, Caprioli RM (2001) Imaging mass spectrometry: a new technology for the analysis of protein expression in mammalian tissues. Nat Med 7:493–496
5. Groseclose MR, Andersson M, Hardesty WM, Caprioli RM (2007) Identification of proteins directly from tissue: in situ tryptic digestions coupled with imaging mass spectrometry. J Mass Spectrom 42:254–262
6. Edwards JL, Kennedy RT (2005) Metabolomic analysis of eukaryotic tissue and prokaryotes using negative mode MALDI time-of-flight mass spectrometry. Anal Chem 77:2201–2209
7. Hattori K, Kajimura M, Hishiki T, Nakanishi T, Kubo A, Nagahata Y, Ohmura M, Yachie-Kinoshita A, Matsuura T, Morikawa T et al (2010) Paradoxical ATP elevation in ischemic penumbra revealed by quantitative imaging mass spectrometry. Antioxid Redox Signal 13:1157–1167
8. Miura D, Fujimura Y, Yamato M, Hyodo F, Utsumi H, Tachibana H, Wariishi H (2010) Ultrahighly sensitive in situ metabolomic imaging for visualizing spatiotemporal metabolic behaviors. Anal Chem 82:9789–9796
9. Harada T, Yuba-Kubo A, Sugiura Y, Zaima N, Hayasaka T, Goto-Inoue N, Wakui M, Suematsu M, Takeshita K, Ogawa K et al (2009) Visualization of volatile substances in different organelles with an atmospheric-pressure mass microscope. Anal Chem 81:9153–9157
10. Cooks RG, Ouyang Z, Takats Z, Wiseman JM (2006) Detection Technologies. Ambient mass spectrometry. Science 311:1566–1570
11. Liu Q, Guo Z, He L (2007) Mass spectrometry imaging of small molecules using desorption/ionization on silicon. Anal Chem 79:3535–3541
12. Nemes P, Barton AA, Vertes A (2009) Three-dimensional imaging of metabolites in tissues under ambient conditions by laser ablation electrospray ionization mass spectrometry. Anal Chem 81:6668–6675
13. Li Y, Shrestha B, Vertes A (2008) Atmospheric pressure infrared MALDI imaging mass spectrometry for plant metabolomics. Anal Chem 80:407–420
14. Sroyraya M, Goto-Inoue N, Zaima N, Hayasaka T, Chansela P, Tanasawet S, Shrivas K, Sobhon P, Setou M (2010) Visualization of biomolecules in the eyestalk of the blue swimming crab, *Portunus pelagicus*, by imaging mass spectrometry using the atmospheric-pressure mass microscope. Surf Interface Anal 42:1589–1592
15. Takizawa Y, Mizuta K, Hayasaka T, Nakanishi H, Okamura J, Mineta H, Setou M (2010) Specific localization of five phosphatidylcholine species in the cochlea by mass microscopy. Audiol Neurootol 16:315–322
16. Sun G, Yang K, Zhao Z, Guan S, Han X, Gross RW (2007) Shotgun metabolomics approach for the analysis of negatively charged water-soluble cellular metabolites from mouse heart tissue. Anal Chem 79:6629–6640
17. Hamada K, Monnai M, Kawai K, Nishime C, Kito C, Miyazaki N, Ohnishi Y, Nakamura M, Suemizu H (2008) Liver metastasis models of colon cancer for evaluation of drug efficacy using NOD/Shi-scid IL2Rγ^{null} (NOG) mice. Int J Oncol 32:153–159
18. Ito M, Hiramatsu H, Kobayashi K, Suzue K, Kawahata M, Hioki K, Ueyama Y, Koyanagi Y, Sugamura K, Tsuji K et al (2002) NOD/SCID/γc^{null} mouse: an excellent recipient mouse model for engraftment of human cells. Blood 100:3175–3182
19. Handa K, Ohmura M, Nishime C, Hishiki T, Nagahata Y, Kawai K, Suemizu H, Nakamura M, Wakui M, Kitagawa Y et al (2010) Phosphorescence-assisted microvascular O_2 measurements reveal alterations of oxygen demand in human metastatic colon cancer in the liver of superimmunodeficient NOG mice. Adv Exp Med Biol 662:423–429
20. Sakuragawa T, Hishiki T, Ueno Y, Ikeda S, Soga T, Yachie-Kinoshita A, Kajimura M, Suematsu M (2010) Hypotaurine is an energy-saving hepatoprotective compound against ischemia–reperfusion injury of the rat liver. J Clin Biochem Nutr 46:126–134
21. Shintani T, Iwabuchi T, Soga T, Kato Y, Yamamoto T, Takano N, Hishiki T, Ueno Y, Ikeda S, Sakuragawa T et al (2009) Cystathionine β-synthase as a carbon monoxide-sensitive regulator of bile excretion. Hepatology 49:141–150
22. Soga T, Baran R, Suematsu M, Ueno Y, Ikeda S, Sakurakawa T, Kakazu Y, Ishikawa T, Robert M, Nishioka T et al (2006) Differential metabolomics reveals ophthalmic acid as an oxidative stress biomarker indicating hepatic glutathione consumption. J Biol Chem 281:16768–16776
23. Kinoshita A, Tsukada K, Soga T, Hishiki T, Ueno Y, Nakayama Y, Tomita M, Suematsu M (2007) Roles of hemoglobin allostery in hypoxia-induced metabolic alterations in erythrocytes: simulation and its verification by metabolome analysis. J Biol Chem 282:10731–10741
24. Accatino L, Simon FR (1976) Identification and characterization of a bile acid receptor in isolated liver surface membranes. J Clin Invest 57:496–508
25. Stahl E, Arnesjo B (1972) Taurocholate metabolism in man. Scand J Gastroenterol 7:559–566
26. Pacifici GM, Rane A (1982) Distribution of UDP-glucuronyltransferase in different human foetal tissues. Br J Clin Pharmacol 13:732–735
27. Suematsu M, Kato S, Ishii H, Asako H, Yanagisawa T, Suzuki H, Oshio C, Tsuchiya M (1991) Intralobular heterogeneity of carbon tetrachloride-induced oxidative stress in perfused rat liver visualized by digital imaging fluorescence microscopy. Lab Invest 64:167–173
28. Ishimoto T, Nagano O, Yae T, Tamada M, Motohara T, Oshima H, Oshima M, Ikeda T, Yagi H, Masuko T, et al. (2011) CD44 variant regulates redox status in cancer cells by stabilizing the xCT subunit of system xc- and thereby promotes tumor growth. Cancer Cell 19:387–400
29. Moscow JA, Fairchild CR, Madden MJ, Ransom DT, Wieand HS, O'Brien EE, Poplack DG, Cossman J, Myers CE, Cowan KH (1989) Expression of anionic glutathione-S-transferase and P-glycoprotein genes in human tissues and tumors. Cancer Res 49:1422–1428
30. Dang DT, Chen F, Kohli M, Rago C, Cummins JM, Dang LH (2005) Glutathione S-transferase pi1 promotes tumorigenicity in HCT116 human colon cancer cells. Cancer Res 65:9485–9494

G Model
ATH-11946; No. of Pages 6
ARTICLE IN PRESS

Atherosclerosis xxx (2011) xxx–xxx

Contents lists available at ScienceDirect

Atherosclerosis

journal homepage: www.elsevier.com/locate/atherosclerosis

Imaging mass spectrometry-based histopathologic examination of atherosclerotic lesions

Nobuhiro Zaima[a,b,*], Takeshi Sasaki[c,d], Hiroki Tanaka[a,e], Xian Wu Cheng[d], Kenji Onoue[a], Takahiro Hayasaka[a], Naoko Goto-Inoue[a], Hirofumi Enomoto[a], Naoki Unno[e], Masafumi Kuzuya[d], Mitsutoshi Setou[a,**]

[a] Department of Cell Biology and Anatomy, Hamamatsu University School of Medicine, 1-20-1, Handayama, Higashi-ku, Hamamatsu, Shizuoka 431-3192, Japan
[b] Department of Applied Biological Chemistry, Kinki University, 3327-204, Naka-machi, Nara 631-8505, Japan
[c] Department of Anatomy and Neuroscience, Hamamatsu University School of Medicine, Japan
[d] Department of Geriatrics, Nagoya University Graduate School of Medicine, Japan
[e] Department of Vascular Surgery, Hamamatsu University School of Medicine, Japan

ARTICLE INFO

Article history:
Received 26 November 2010
Received in revised form 18 March 2011
Accepted 30 March 2011
Available online xxx

Keywords:
ApoE-deficient mouse
Lipids
Smooth muscle cells
Arachidonic acid
Phosphatidylcholine
Imaging mass spectrometry

ABSTRACT

Aims: Imaging mass spectrometry (IMS) enables the visualization of individual molecules present on tissue sections. We attempted to identify and visualize specific markers for aortic atherosclerotic lesions.
Methods and results: Atherosclerotic lesions were obtained from aortic roots of apolipoprotein E (ApoE)-deficient mice at 60 weeks of age and from femoral arteries of humans with peripheral artery occlusive disease. IMS was performed with a matrix-assisted laser desorption/ionization mass spectrometry time-of-flight (TOF)/TOF-type instrument. The molecular ions at m/z 671.6 and 673.6 were found to be specific molecules in the mouse and human lipid-rich regions. These molecules were assigned as cholesterol linoleate (CE 18:2) and cholesterol oleate (CE 18:1). In the case of the human samples, triacylglycerol was also localized in the lipid-rich regions. The distributions of the molecular ions at m/z 804.5 and 832.5 were the same as the distribution of both the mouse and the human SMCs. These molecules were assigned as phosphatidylcholine (PC) (diacyl 16:0/20:4) and PC (diacyl 18:0/20:4). The molecular ion at m/z 566.9 was localized in the mouse calcified regions, and the molecular ions at m/z 539.0 were localized in the human calcified regions.
Conclusions: The IMS-based histopathologic examination (IbHE) revealed the characteristic peaks of lipid-rich regions, SMCs, and calcified regions in the atherosclerotic lesions. In addition, IbHE revealed the characteristic distribution of lipids in human atherosclerotic lesions. These data indicate that an IMS-based pathologic approach is of considerable value as a new histopathologic examination.

1. Introduction

Atherosclerosis is a progressive and multigenic vascular disease that involves plaque formation in intimal areas that include various cells and molecules. The development of an atherosclerotic plaque is reported to be closely associated with dyslipidemia and chronic inflammation [1]. The increased permeability of the vascular endothelium causes the intimal accumulation of oxidized low-density lipoprotein (LDL) [2]. Monocytes that are recruited to the intima and subintima transform into macrophages and foam cells through the increased uptake of modified LDL, thereby leading to the formation of early atherosclerotic lesions (fatty streaks) [1]. Fatty streaks grow into atherosclerotic plaques following the accumulation of inflammatory cells and the evolution of a lipid core region that is surrounded by a cap of smooth muscle cells (SMCs) [3,4]. In the lipid-rich atherosclerotic plaques, such as macrophages or SMCs occurs, and these apoptotic cells form a necrotic core [5]. The persistence of these processes finally leads to vascular calcification and rupture of the plaque [6]. The development of atherosclerosis is accompanied by the progressive alteration of the vascular walls [7]. Therefore, it is important to examine the condition of the vascular walls to estimate the pathology of atherosclerosis. Conventional stainings such as oil staining or immunostaining are essential for examination of the pathologic process of atherosclerosis. However, conventional stainings have 3 weaknesses. The first is that conventional oil staining can-

* Corresponding author at: Department of Applied Biological Chemistry, Kinki University, 3327-204, Naka-machi, Nara 631-8505, Japan. Tel.: +81 742 43 8067; fax: +81 742 43 8067.
** Corresponding author. Tel.: +81 53 435 2292; fax: +81 53 435 2292.
E-mail addresses: zaimanobuhiro@gmail.com (N. Zaima), setou@hama-med.ac.jp (M. Setou).

0021-9150/$ – see front matter © 2011 Elsevier Ireland Ltd. All rights reserved.
doi:10.1016/j.atherosclerosis.2011.03.044

Please cite this article in press as: Zaima N, et al. Imaging mass spectrometry-based histopathologic examination of atherosclerotic lesions. Atherosclerosis (2011), doi:10.1016/j.atherosclerosis.2011.03.044

not visualize the species of lipids that are strongly involved in the development of atherosclerosis. Although cholesterols are considered the predominant accumulated materials in atherosclerotic lesions [8], we recently found characteristic aortic atherosclerotic lesions that accumulate triglycerides (TG) and show normal cholesterol levels [9]. This finding emphasizes the necessity of establishing an examination method that enables the selective visualization of lipids in atherosclerotic lesions. The second weakness is that immunostaining requires several antibodies or sections for the multistaining procedure. The number of sections available is often limited in cases in which local lesions are examined. The third weakness is that immunostaining often cannot detect the low-molecular compounds such as metabolites. Therefore, the simultaneous visualization of biomolecules and component cells in atherosclerotic vascular disease would be useful for the pathologic examination of atherosclerotic lesions.

Imaging mass spectrometry (IMS) is expected to be a suitable tool for investigating the pathologic conditions of atherosclerotic vascular disease. IMS enables the visualization of individual molecules on tissue sections, without requiring antibodies, staining, or complicated pretreatment steps [10,11]. IMS allows the detection of a wide range of biomolecules, such as lipids [12–16], glycolipids [17,18], and proteins [19,20], as well as nutrients [21,22]. In this study, we attempted to identify and visualize specific markers for aortic atherosclerotic lesions using an IMS-based histopathologic examination (IbHE).

2. Materials and methods

2.1. Chemicals and reagents

2,5-Dihydroxybenzoic acid (DHB) was purchased from Bruker Daltonics (Bremen, Germany). All chemicals used in this study were of the highest purity available.

2.2. Ethics

This study was approved by the Ethics Committee of Clinical Research, Hamamatsu University School of Medicine.

2.3. Animals

All animal experiments were performed in accordance with the guidelines of Hamamatsu University School of Medicine for Animal Care. Male ApoE-deficient mice with a C57BL/6 genetic background were obtained from the Jackson Laboratory (Bar Harbor, ME). The mice were provided with a standard diet (Oriental Yeast, Tokyo, Japan) and tap water ad libitum.

2.4. Tissue collection and processing

The mice (age, 60 or 12 weeks) were euthanized by an intraperitoneal pentobarbital injection, and were perfused through the left cardiac ventricle with isotonic saline and 4% paraformaldehyde in a 0.01 mol/L phosphate buffer, pH 7.4, under physiological pressure. The aortic roots were removed and immersed in fixative (4% paraformaldehyde in a 0.01 mol/L phosphate buffer, pH 7.4) for 16 h (4 °C), and then, the samples were embedded in 2% carboxymethyl cellulose (CMC) and frozen in isopentane, which was chilled in liquid nitrogen. Common femoral arteries were harvested from male patients with peripheral artery occlusive disease (PAD) who underwent femoro-popliteal bypass surgery for atherosclerotic samples. After perivascular adipose tissues were carefully removed, femoral arteries were frozen in isopentane without any fixation. Samples were prepared as previously described [23], but with slight modifications. In brief, consecutive 8-μm sections were obtained using a cryostat (CRYOCUT CM 1850; Leica Microsystems, Wetzlar, Germany). The serial sections were mounted onto MAS-coated slides (Matsunami, Osaka, Japan) for histochemical and immunohistochemical staining, and indium-tin oxide (ITO)-coated glass slides (Bruker Daltonics) for imaging mass spectrometry.

2.5. Histochemical and immunohistochemical staining

The serial sections were stained with oil red O for the visualization of lipids. The corresponding sections on separate slides were used for the immunohistochemical staining, using rabbit polyclonal antibody against α-SMC actin (1:50, Thermo Fisher Scientific, CA, USA) for visualization of SMCs. The sections were preincubated with 3% normal goat serum (Vector Laboratories, MI) and then incubated with primary antibodies for 45 min at room temperature. The sections were then reacted with horseradish peroxidase (HRP)-conjugated secondary antibody against rabbit IgG (1:100, Vector Laboratories) for 45 min at room temperature. These sections were visualized with an HRP substrate kit (Vector Laboratories) according to the manufacturer's instructions. The counterstaining for the nucleus was performed with Mayer's hematoxylin.

2.6. IMS

50 mg/mL DHB in methanol/water (7/3, v/v) was used as a matrix. A total of 500 μL DHB matrix solution was sprayed uniformly over the sections with a 0.2-mm nozzle caliber airbrush (Procon Boy FWA Platinum; Mr. Hobby, Tokyo, Japan). After the slide glass was dried, it was affixed to the mass spectrometer target plate. IMS was performed using a matrix-assisted laser desorption/ionization mass spectrometry (MALDI) time of flight (TOF)/TOF-type instrument (Ultraflex II, Bruker Daltonics) equipped with a 355-nm Nd:YAG laser at a repetition rate of 200 Hz. Data were acquired with a step size of 25 μm for mice samples or 50 μm for human samples in the positive ion mode (reflector mode). The m/z values in the range of 400–1000 were measured. The laser diameter was set to the minimum size. The m/z values were calibrated externally using a peptide calibration standard (Bruker Daltonics). All the spectra were acquired automatically using FlexImaging software (Bruker Daltonics). Normalization of spectra based on total ion current (TIC) was also performed using this software to compare the different samples. The software was also used to create two-dimensional ion-density maps, and peak analyses were performed using FlexAnalysis (Bruker Daltonics). After analysis by IMS, the sections were subjected to hematoxylin–eosin (HE) staining.

2.7. Molecular identification

Phosphatidylcholine (PC) and TG were identified by tandem MS (MS/MS) [24]. MS/MS was performed using a MALDI linear quadrupole ion-trap-type instrument (LTQ-XL, Thermo Fisher Scientific) because neutral loss of fatty acids could not be detected by MS/MS using MALDI time of flight (TOF)/TOF-type instrument. The precursor and fragment ions obtained by collision-induced dissociation were ejected from the ion trap and analyzed. The collision energy was set to 30%. The laser energy was set to 30 μJ. Cholesterol ester (CE) was assigned on the basis of m/z value.

3. Results

Fig. 1a is an HE staining image of an aortic root of ApoE-deficient mouse at 60 weeks of age. We fractionated 3 regions according to the pathologic findings. Region 1 is a lipid-rich region with an insubstantial cell component. This region was positively stained by oil red O staining (Fig. 1b). Region 2 is located in the media and

Please cite this article in press as: Zaima N, et al. Imaging mass spectrometry-based histopathologic examination of atherosclerotic lesions. Atherosclerosis (2011), doi:10.1016/j.atherosclerosis.2011.03.044

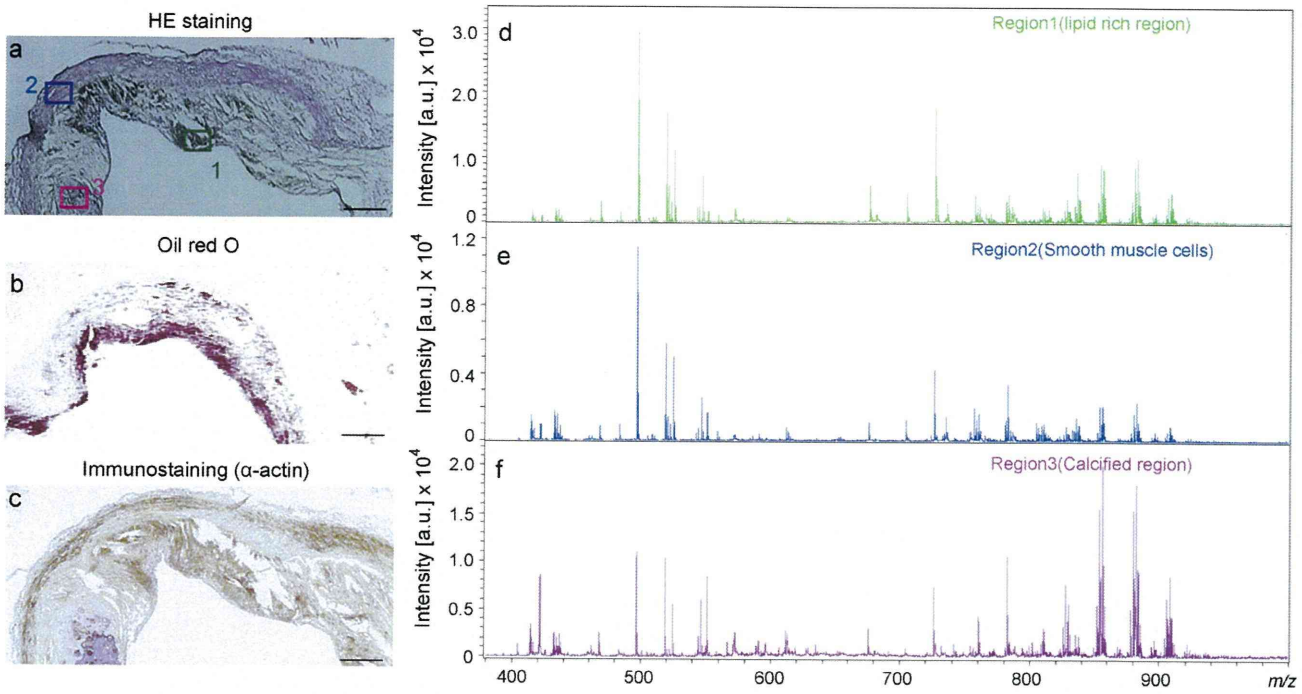

Fig. 1. The optical images and mass spectra of aortic root of ApoE-deficient mouse at 60 weeks of age. HE staining that has been stained after IMS (a). Scale bar: 100 μm. Region 1 is the lipid-rich region, region 2 is the SMCs, and region 3 is the calcified region. Oil red O staining (b). The immunostaining of α-actin, which is a marker for SMCs (c). The mass spectrum of region 1 (d), region 2 (e), and region 3 (f).

adventitia, which positively stained for the SMC marker α-actin (Fig. 1c). Region 3 is a calcified region in which chondrocytes were observed upon HE staining and immunostaining (Fig. 1a and c). Fig. 1d–f shows mass spectra obtained from all 3 regions. These mass spectra differ among the 3 regions, suggesting that a specific marker for each region could be found by comparing the 3 mass spectra.

We found 5 *m/z* values that were characteristic for the 3 regions. The molecules at *m/z* 671.6 and *m/z* 673.6 were specific for the lipid-rich region (Fig. 2a and b). These peaks were assigned as CE (18:2) and CE (18:1) on the basis of the *m/z* value. These 2 molecules showed the similar distribution. We made these images combine into a single color (Fig. 2c). The distribution of molecules at *m/z* 804.5 and *m/z* 832.5 were the same as the distribution of SMCs (Fig. 2d and e). The molecular ions at *m/z* 804.5 and 832.5 were assigned as PC (diacyl 16:0/20:4) and PC (diacyl 18:0/20:4) by MS/MS on tissue (Supplementary Fig. 1). PC was found to be dominantly detected as sodium adducted positive ion on the paraformaldehyde-fixed tissues (Supplementary Fig. 1). These 2 molecules showed the similar distribution. We made these images combine into a single color (Fig. 2f). We confirmed that the distribution of SMCs was not the same as the distribution of the other major PC species, such as PC (diacyl 16:0/16:0), PC (diacyl 16:0/18:0), PC (diacyl 16:0/18:1), PC (diacyl 16:0/18:2), PC (diacyl 18:0/18:0), PC (diacyl 18:0/18:1), and PC (diacyl 18:0/18:2) (Supplementary Fig. 2). The molecule at *m/z* 566.9 was specific for the calcified region (Fig. 2g). The monochrome image of *m/z* 566.9 is shown in Fig. 2h. The HE staining image and the merge image of each of the 3 regions are shown in Fig. 2i and j. These data indicated that we could distinguish the 3 regions by IbHE. The mass spectra of 3 regions are shown in Supplemental Fig. 3 and we confirmed that the distribution of other detected peaks in our experimental condition were different from 3 region (data not shown). Fig. 2k–m are images of aortic roots of ApoE deficient mice at 12 weeks of age. We used these aortic roots as non-atherosclerotic aortic roots because intimal thickening and lipid rich region were not observed in these samples (Fig. 2k and l). SMCs were observed in these samples (Fig. 2m). CE (18:2), CE (18:1), PC (diacyl 16:0/20:4), PC (diacyl 18:0/20:4) and *m/z* 566.9 were not detected by the analyses of these samples (Fig. 2n–p). These results suggest that CE (18:2), CE (18:1), PC (diacyl 16:0/20:4), PC (diacyl 18:0/20:4) and *m/z* 566.9 are the potential marker of atherosclerotic aortic roots of ApoE deficient mice. The identified potential marker list of aortic roots of the ApoE-deficient mice is summarized in Table 1.

We investigated whether the biomarkers of the mouse atherosclerotic aortae could be used to analyze the human atherosclerotic femoral arteries (Fig. 3). The distribution of CE (18:2) and CE (18:1) were partly the same as that of the oil red O positive region (Fig. 3a–d). The distribution of PC (diacyl 16:0/20:4) and PC (diacyl 18:0/20:4) were the same as the distribution of SMCs (Fig. 3e–h). The molecule at *m/z* 566.9 was not detected in the human samples (Fig. 3i–k). In the case of the human samples, the localization of the molecule at *m/z* 539.0 was the same as that of the calcified region (data not shown). The HE staining image and the merge image of the 3 regions are shown in Fig. 3l and m. We next investigated the distribution of lipid species because the distribution of CE was not completely the same as that of the region positively stained by oil red O staining. We found that there was TG (18:0/18:1/18:2) in the human atherosclerotic femoral arteries (Fig. 3o). The region where TG was detected was positively stained by oil red O staining (Fig. 3o ROI1). Adipocytes were not observed in the region where TG was detected. The characteristic distribution of TG (18:0/18:1/18:2) and CE is shown in Fig. 3q. The merge

Table 1
Identified potential marker list of mouse atherosclerotic lesion region.

Region	*m/z*	Assignment
Lipid rich region	671.6	CE (18:2)
	673.6	CE (18:1)
Smooth muscle cell	804.5	PC (diacyl 16:0/20:4)
	832.5	PC (diacyl 18:0/20:4)

Please cite this article in press as: Zaima N, et al. Imaging mass spectrometry-based histopathologic examination of atherosclerotic lesions. Atherosclerosis (2011), doi:10.1016/j.atherosclerosis.2011.03.044

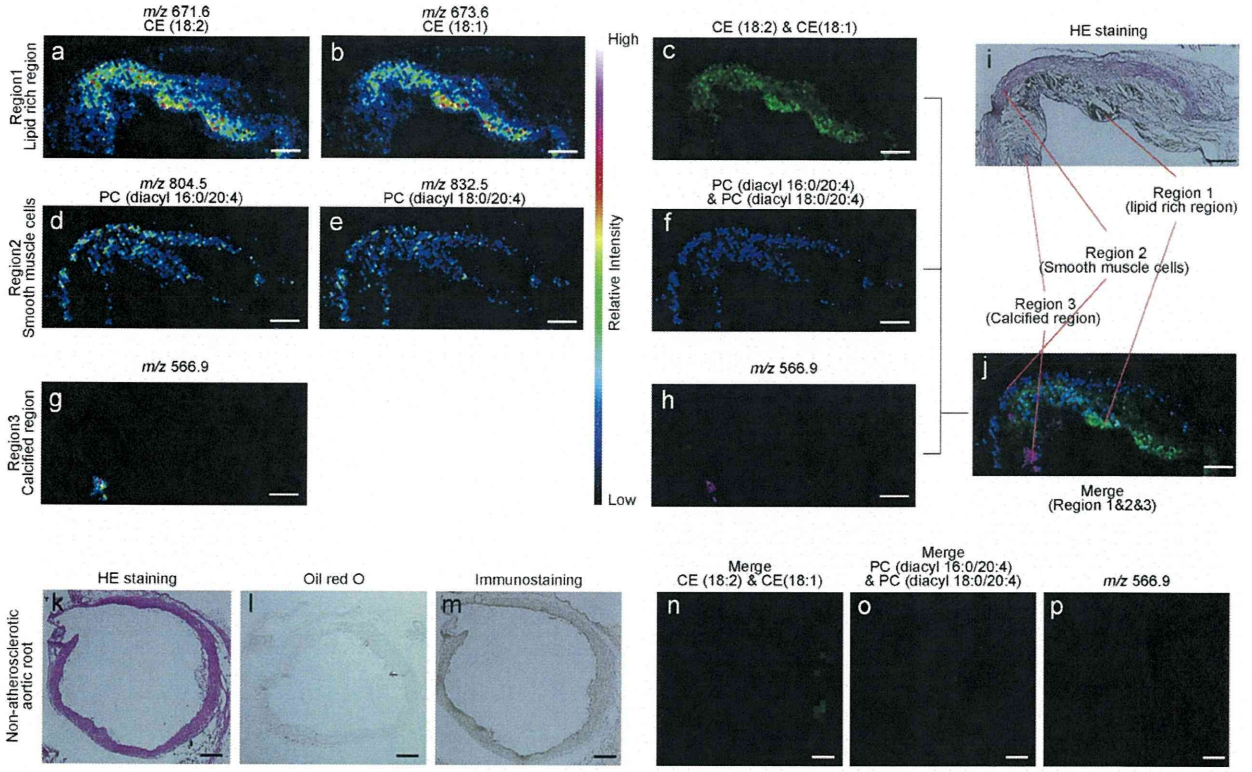

Fig. 2. The representative specific molecule images of a mouse atherosclerotic lesion. Scale bar: 100 μm. The specific ion images of region 1 (a and b) and the combined image of *m/z* 671.6 and 673.6 (c) ($n = 3$). The specific ion images of region 2 (d and e) and the combined image of *m/z* 804.5 and 832.5 (f) ($n = 3$). The specific ion images of region 3 (g) and the monochrome image of *m/z* 566.9 (h) ($n = 3$). The comparison of HE staining (i) and the merge images of regions 1–3 (j). The image of non-atherosclerotic aortic roots of mice at 12 weeks of age ($n = 3$) (k–m). Scale bar: 200 μm. HE staining that has been stained after IMS (k). Oil red O staining (l). The immunostaining of α-actin, which is a marker for SMCs (m). The merge image of CE (18:2) and CE (18:1) (n). The merge image of PC (diacyl 16:0/20:4) and PC (diacyl 18:0/20:4) (o). The ion image of *m/z* 566.9 (p).

image of TG and CE was the same as that of the oil red O positive stained region. The identified potential marker list for human atherosclerotic femoral arteries is summarized in Table 2.

4. Discussion

In this study, we were able to find and identify the characteristic molecules of atherosclerotic lesions in ApoE-deficient mice and humans, which indicated that our approach can be applied to the pathologic assessment of such lesions. Various cells and molecules that may be associated with plaque development and vulnerability are included in the atheroma. The mass spectra obtained from the lipid-rich region, the SMCs, and the calcified regions were different from each other (Fig. 1). This was because the mass spectra obtained by IMS reflected the profiles of their metabolites. We found specific molecules of atherosclerotic lesion of ApoE KO mouse (Fig. 2). The results obtained in Fig. 2 supported the existence of a real capacity of the spectra to differentiate between their pathologic conditions. CE (18:2) and CE (18:1) were specific for the lipid-rich regions of the mouse samples (Fig. 2a–c). These results were reasonable because CE was accumulated in the atherosclerotic plaque. PC (diacyl 16:0/20:4) and PC (diacyl 18:0/20:4) were found to be characteristic biomolecules of the SMCs in atherosclerotic lesions. It is of interest that the PCs that contain arachidonic acid (20:4) are the specific biomolecules of the SMCs. Arachidonic acid is a precursor of lipid mediators such as leukotriene (LT) and prostaglandin (PG), which induce inflammation [25]. The role of arachidonic acid in SMCs was not previously established. Therefore, it is of interest to clarify the role of PC (diacyl 16:0/20:4) and PC (diacyl 18:0/20:4) in SMCs. Because PC (diacyl 16:0/20:4) and PC (diacyl 18:0/20:4) were not detected in SMCs of non-atherosclerotic aortic roots of ApoE KO mice, we speculated PC (diacyl 16:0/20:4) and PC (diacyl 18:0/20:4) might play undesirable roles in the development of atherosclerotic lesions. The molecule at *m/z* 566.9 was specific for the calcified regions in our mice samples (Fig. 2g). We could not identify this molecule. In our opinion, this result does not compromise the intended histopathologic use of our approach, since the distinctions were valid even if the assignments were uncertain. However, further studies should be needed to identify the molecule at *m/z* 566.9 to enhance basic understanding of heart disease.

In the case of human atherosclerotic lesions, the distribution of PC (diacyl 16:0/20:4) and PC (diacyl 18:0/20:4) were the same as the distribution of SMCs (Fig. 3e–h). The specific biomolecules for the human calcified regions were not the same as those for the mouse calcified regions (Figs. 2J and 3m). This may be because the species differed or because there was a mature degree of calcification in the calcified regions. We found that CE and TG were localized in the lipid-rich regions of the human atherosclerotic lesions (Fig. 3o–q). Interestingly, the distributions of CE and TG were different from each another (Fig. 3q). TG was observed as intracellular

Table 2
Identified potential marker list of human atherosclerotic lesion region.

Region	*m/z*	Assignment
Lipid rich region	671.6	CE (18:2)
	673.6	CE (18:1)
	907.7	TG (18:0/18:1/18:2)
Smooth muscle cell	804.5	PC (diacyl 16:0/20:4)
	832.5	PC (diacyl 18:0/20:4)

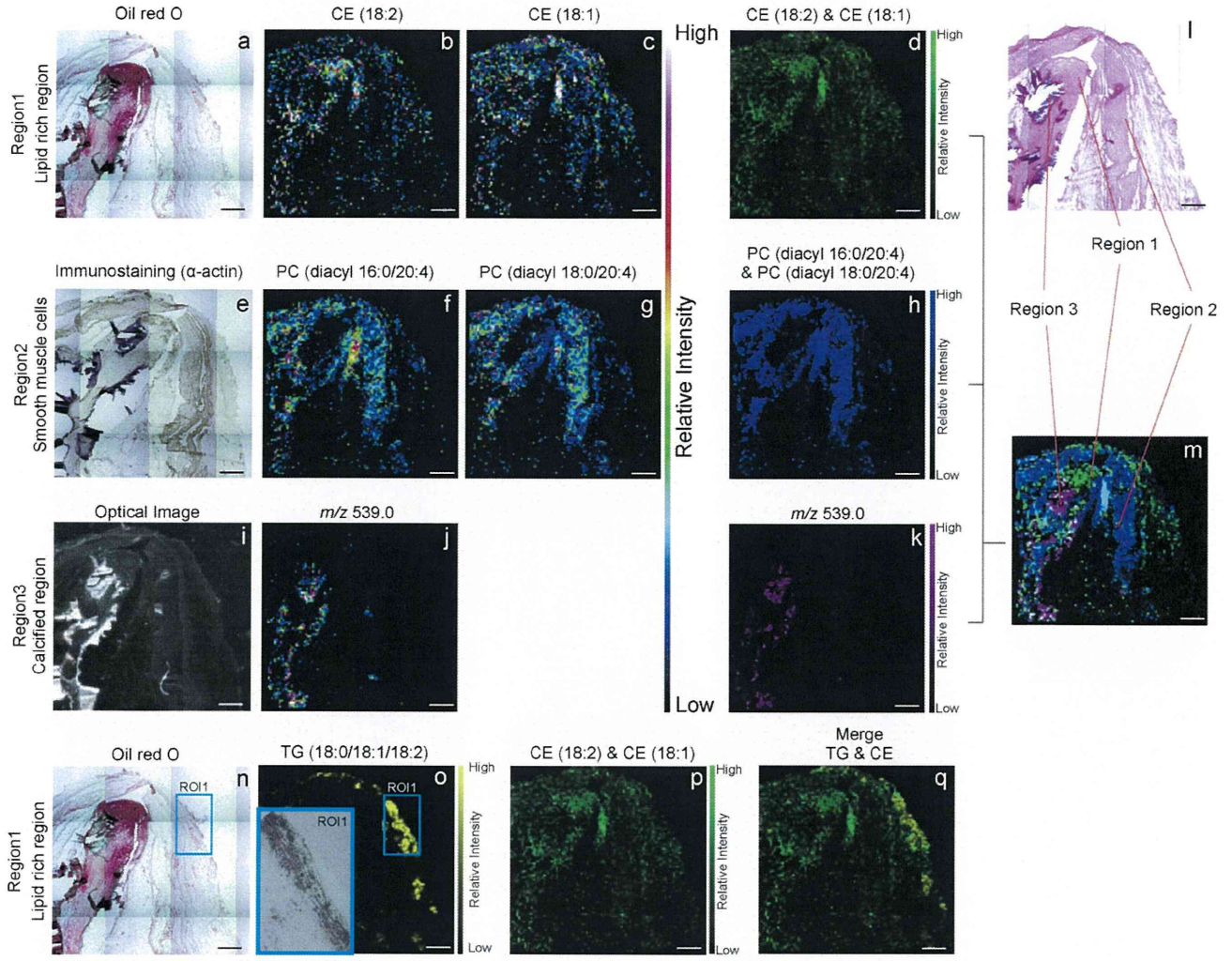

Fig. 3. The representative specific molecule images of a human atherosclerotic lesion ($n = 6$). Scale bar: 1000 μm. Oil red O staining (a and n). The ion images of CE (18:2) and CE (18:1) (b and c) and the combined monochrome images (d and p). The immunostaining of α-actin, which is a marker for SMCs (e). The ion images of PC (diacyl 16:0/20:4) and PC (diacyl 18:0/20:4) (f and g) and the combined monochrome images (h). The optical image of the analyzed sample (i). The ion image of *m/z* 539.0 (j) and the monochrome image (k). The comparison of HE staining (l) and the merge images of regions 1–3 (m). Consecutive sections are used in oil red O staining and immunostaining. The distribution of TG (18:0/18:1/18:2) (o). ROI1: high power field of oil red O staining. The merge image of TG and CE (q).

lipid droplets (Fig. 3o ROI1). Although the role of TG in the evolution of atherosclerosis remains unknown, there is a possibility that TG plays an important role in the evolution of atherosclerosis, as we previously found the characteristic phenotype that accumulates TG in aortic atherosclerotic lesions, while accumulated cholesterol level was normal [9]. It is reported that EPA ethyl ester, which is a drug used to reduce serum TG levels, decreases the incidence of coronary events in hypercholesterolemia with impaired glucose metabolism [26]. The mechanism of action of EPA ethyl ester may be involved in the TG in atherosclerotic lesions. The reanalysis of human atherosclerotic lesions by IbHE may be an important way to clarify the role of TG in the development of atherosclerosis.

5. Conclusion

We detected specific molecular markers for atherosclerotic lesions in ApoE-deficient mice and in humans by using IbHE, indicating that specific peaks can be likened to antigens in immunostaining. Because IMS can detect numerous peaks that reflect the metabolic profile of optional regions (Fig. 1d–f), several characteristic peaks of the regions of interest can be identified. Therefore, this approach conceptually distinguishes all atherosclerotic components on basis of the combination of characteristic peaks. Since many factors are involved in the development of atherosclerosis [27–29], a larger-scale study to identify the specific molecules of other atherosclerotic lesion components, such as leukocytes, is necessary. In addition, a reexamination of vascular disease by IbHE might elucidate new findings, because IbHE can visualize the localization of low molecular weight molecules, which are rarely visualized by other techniques. At this time, IMS is the only method for the specific and simultaneous visualization of lipids in tissue sections. Lipids are considered strong risk factors for atherosclerosis. Therefore, many clinical trials specifically targeted serum lipid control in order to develop treatments for atherosclerotic diseases. We speculate that the accumulated lipids in atherosclerotic lesions do not belong to a single lipid species such as CE. Determining the localization and class of lipids in atherosclerotic lesions by using IbHE can be an important tool for the pathologic analysis of such lesions. One limitation of our approach is spatial resolution. The spatial resolution of IMS is limited to >10 μm at this time [30]. Therefore, a combination of

Please cite this article in press as: Zaima N, et al. Imaging mass spectrometry-based histopathologic examination of atherosclerotic lesions. Atherosclerosis (2011), doi:10.1016/j.atherosclerosis.2011.03.044

conventional staining and IbHE is essential for a successful micron-order analysis.

Disclosures

We have no potential conflicts of interest to report for any of the funding listed above. We include 2 tables and 3 figures in the paper (3 figures destined to on line only supplementary material).

Sources of funding

This work was supported by the Program for Promotion of Basic and Applied Researches for Innovations in Bio-oriented Industry (BRAIN) and a Grant-in-Aid for Scientific Research (C) (22590522) to N.Z.

Acknowledgment

We would like to thank Mayumi Suzuki for her technical assistance.

Appendix A. Supplementary data

Supplementary data associated with this article can be found, in the online version, at doi:10.1016/j.atherosclerosis.2011.03.044.

References

[1] Weber C, Zernecke A, Libby P. The multifaceted contributions of leukocyte subsets to atherosclerosis: lessons from mouse models. Nat Rev Immunol 2008;8:802–15.
[2] Hansson GK. Inflammation, atherosclerosis, and coronary artery disease. N Engl J Med 2005;352:1685–95.
[3] Doran AC, Meller N, McNamara CA. Role of smooth muscle cells in the initiation and early progression of atherosclerosis. Arterioscler Thromb Vasc Biol 2008;28:812–9.
[4] Virmani R, Burke AP, Farb A, Kolodgie FD. Pathology of the vulnerable plaque. J Am Coll Cardiol 2006;47:C13–8.
[5] Tabas I. Macrophage apoptosis in atherosclerosis: consequences on plaque progression and the role of endoplasmic reticulum stress. Antioxid Redox Signal 2009;11:2333–9.
[6] Aikawa M, Libby P. The vulnerable atherosclerotic plaque: pathogenesis and therapeutic approach. Cardiovasc Pathol 2004;13:125–38.
[7] Ross R. Atherosclerosis—an inflammatory disease. N Engl J Med 1999;340:115–26.
[8] Goldstein JL, Brown MS. Familial hypercholesterolemia: identification of a defect in the regulation of 3-hydroxy-3-methylglutaryl coenzyme a reductase activity associated with overproduction of cholesterol. Proc Natl Acad Sci USA 1973;70:2804–8.
[9] Hirano K, Ikeda Y, Zaima N, Sakata Y, Matsumiya G. Triglyceride deposit cardiomyovasculopathy. N Engl J Med 2008;359:2396–8.
[10] Cornett DS, Reyzer ML, Chaurand P, Caprioli RM. Maldi imaging mass spectrometry: molecular snapshots of biochemical systems. Nat Methods 2007;4:828–33.
[11] Zaima N, Hayasaka T, Goto-Inoue N, Setou M. Matrix-assisted laser desorption/ionization imaging mass spectrometry. Int J Mol Sci 2010;11:5041–56.
[12] Touboul D, Piednoel H, Voisin V, et al. Changes of phospholipid composition within the dystrophic muscle by matrix-assisted laser desorption/ionization mass spectrometry and mass spectrometry imaging. Eur J Mass Spectrom (Chichester, Eng) 2004;10:657–64.
[13] Hayasaka T, Goto-Inoue N, Sugiura Y, et al. Matrix-assisted laser desorption/ionization quadrupole ion trap time-of-flight (Maldi-Qit-Tof)-based imaging mass spectrometry reveals a layered distribution of phospholipid molecular species in the mouse retina. Rapid Commun Mass Spectrom 2008;22:3415–26.
[14] Murphy RC, Hankin JA, Barkley RM. Imaging of lipid species by Maldi mass spectrometry. J Lipid Res 2009;50:S317–22.
[15] Zaima N, Goto-Inoue N, Adachi K, Setou M. Selective analysis of lipids by thin-layer chromatography blot matrix-assisted laser desorption/ionization imaging mass spectrometry. J Oleo Sci 2011;60:93–8.
[16] Zaima N, Matsuyama Y, Setou M. Principal component analysis of direct matrix-assisted laser desorption/ionization mass spectrometric data related to metabolites of fatty liver. J Oleo Sci 2009;58:267–73.
[17] Goto-Inoue N, Hayasaka T, Zaima N, Setou M. The specific localization of seminolipid molecular species on mouse testis during testicular maturation revealed by imaging mass spectrometry. Glycobiology 2009;19:950–7.
[18] Colsch B, Woods AS. Localization and imaging of sialylated glycosphingolipids in brain tissue sections by Maldi mass spectrometry. Glycobiology 2010;20:661–7.
[19] Groseclose MR, Andersson M, Hardesty WM, Caprioli RM. Identification of proteins directly from tissue: in situ tryptic digestions coupled with imaging mass spectrometry. J Mass Spectrom 2007;42:254–62.
[20] Stoeckli M, Chaurand P, Hallahan DE, Caprioli RM. Imaging mass spectrometry: a new technology for the analysis of protein expression in mammalian tissues. Nat Med 2001;7:493–6.
[21] Goto-Inoue N, Setou M, Zaima N. Visualization of spatial distribution of gamma-aminobutyric acid in eggplant (*Solanum Melongena*) by matrix-assisted laser desorption/ionization imaging mass spectrometry. Anal Sci 2010;26:821–5.
[22] Zaima N, Goto-Inoue N, Hayasaka T, Setou M. Application of imaging mass spectrometry for the analysis of Oryza Sativa rice. Rapid Commun Mass Spectrom 2010;24:2723–9.
[23] Zaima N, Hayasaka T, Goto-Inoue N, Setou M. Imaging of metabolites by Maldi mass spectrometry. J Oleo Sci 2009;58:415–9.
[24] Hayasaka T, Goto-Inoue N, Zaima N, Kimura Y, Setou M. Organ-specific distributions of lysophosphatidylcholine and triacylglycerol in mouse embryo. Lipids 2009;44:837–48.
[25] Kuehl Jr FA, Egan RW. Prostaglandins, arachidonic acid, and inflammation. Science 1980;210:978–84.
[26] Oikawa S, Yokoyama M, Origasa H, et al. Suppressive effect of epa on the incidence of coronary events in hypercholesterolemia with impaired glucose metabolism: sub-analysis of the Japan Epa lipid intervention study (Jelis). Atherosclerosis 2009;206:535–9.
[27] Laxton RC, Hu Y, Duchene J, et al. A role of matrix metalloproteinase-8 in atherosclerosis. Circ Res 2009;105:921–9.
[28] Zakkar M, Chaudhury H, Sandvik G, et al. Increased endothelial mitogen-activated protein kinase phosphatase-1 expression suppresses proinflammatory activation at sites that are resistant to atherosclerosis. Circ Res 2008;103:726–32.
[29] Paulson KE, Zhu SN, Chen M, et al. Resident intimal dendritic cells accumulate lipid and contribute to the initiation of atherosclerosis. Circ Res 2010;106:383–90.
[30] Harada T, Yuba-Kubo A, Sugiura Y, et al. Visualization of volatile substances in different organelles with an atmospheric-pressure mass microscope. Anal Chem 2009;81:9153–7.

Please cite this article in press as: Zaima N, et al. Imaging mass spectrometry-based histopathologic examination of atherosclerotic lesions. Atherosclerosis (2011), doi:10.1016/j.atherosclerosis.2011.03.044

ARTICLE IN PRESS

BBAMCB-57068; No. of pages: 9; 4C: 4, 5, 6, 7

Biochimica et Biophysica Acta xxx (2011) xxx–xxx

Contents lists available at ScienceDirect

Biochimica et Biophysica Acta

journal homepage: www.elsevier.com/locate/bbalip

Review

Imaging mass spectrometry for lipidomics ☆

Naoko Goto-Inoue [a], Takahiro Hayasaka [a], Nobuhiro Zaima [b], Mitsutoshi Setou [a,*]

[a] Department of Molecular Anatomy, Molecular Imaging Frontier Research Center, Hamamatsu University School of Medicine, 1-20-1 Handayama, Higashi-ku, Hamamatsu, Shizuoka 431-3192, Japan

[b] Department of Applied Biological Chemistry, Graduate School of Agriculture, Kinki University, Japan

ARTICLE INFO

Article history:
Received 14 December 2010
Received in revised form 15 March 2011
Accepted 16 March 2011
Available online xxxx

Keywords:
Lipidomics
Imaging mass spectrometry
Matrix-assisted laser desorption/ionization

ABSTRACT

Matrix-assisted laser desorption/ionization mass spectrometry (MALDI-MS) is a powerful tool that enables the simultaneous detection and identification of biomolecules in analytes. MALDI-imaging mass spectrometry (MALDI-IMS) is a two-dimensional MALDI-MS technique used to visualize the spatial distribution of biomolecules without extraction, purification, separation, or labeling of biological samples. This technique can reveal the distribution of hundreds of ion signals in a single measurement and also helps in understanding the cellular profile of the biological system. MALDI-IMS has already revealed the characteristic distribution of several kinds of lipids in various tissues. The versatility of MALDI-IMS has opened a new frontier in several fields, especially in lipidomics. In this review, we describe the methodology and applications of MALDI-IMS to biological samples. This article is part of a Special Issue entitled: Lipodomics and Imaging Mass Spectrometry.

1. Introduction

Lipids comprise a wide range of molecules such as fatty acids, glycerolipids, glycerophospholipids, sphingolipids, etc. These lipids have a wide range of biological functions, and each cell type exhibits a different lipid composition and distribution. For comprehensive lipid analyses, we use a "lipidomics" approach, which provides further insights into complex metabolic networks of biological systems. Mainly, lipidomics approaches have been demonstrated by the use of mass spectrometry (MS) to perform full characterization of lipid molecular species [1–4]. Qualitative and quantitative knowledge of the lipid composition is the first step for lipidomics. The most widely used MS instrument is MS coupled with liquid chromatography (LC)–electrospray ionization (ESI) [4]. LC–ESI–MS can quantify the amounts of lipids as well as identify the structure of lipid molecules. Many reports have shown that shot-gun lipidomics analyses are the most suitable analytical method to investigate the full range of lipid molecules in cells or tissues or to find molecular-level indications of diseases by comparing the distribution of various lipid molecules in diseased tissue with that in control samples [5,6]. However, this technique entails extraction and purification steps, leading to the loss of the lipid distribution over the biological tissue. Meanwhile, numerous techniques of chemical imaging enable the detection and the localization of lipids. Staining with Nile Red, Oil Red O [7], osmium tetroxide [8], or BODIPY is a common method to localize the lipid fraction on frozen sections, whereas few specific lipid antibodies [9] are commercially available. These approaches target either the complete lipid fraction or only one specific family, not molecular species with a wide variety of fatty acid compositions. By contrast, imaging mass spectrometry (IMS) is a relatively new imaging method based on MS. IMS is a two-dimensional MS technique used to visualize the spatial distribution of biomolecules. Several ionization methods, including secondary ion mass spectrometry (SIMS), desorption electrospray ionization (DESI), laser ablation electrospray ionization (LAESI), nanostructure-initiator (NI), and matrix-assisted laser desorption/ionization (MALDI), have been investigated as methods of IMS. In this review, we focus on lipid imaging by MALDI-MS because MALDI-IMS is the most common IMS method for lipid imaging. Indeed, the versatility of MALDI-IMS has opened a new frontier in several other fields, as well as lipidomics.

2. Instruments for IMS

IMS is a remarkable technology that enables us to determine the distribution of biological molecules present in tissue sections by direct ionization and detection. This technique is now widely used for in situ imaging of endogenous or exogenous molecules. There are several kinds of instruments used for IMS.

2.1. Ionization methods for IMS

IMS techniques include various ionization methods that can ionize the analytes on the surface, such as SIMS [10–13], DESI [14–18], LAESI [19,20], NI [21,22], and MALDI [23–25]. These ionization methods have both merits and demerits; therefore, users have to consider carefully which method is best for their analyses.

☆ This article is part of a Special Issue entitled: Lipodomics and Imaging Mass Spectrometry.

* Corresponding author. Tel./fax: +81 53 435 2292.
E-mail address: setou@hama-med.ac.jp (M. Setou).

1388-1981/$ – see front matter © 2011 Elsevier B.V. All rights reserved.
doi:10.1016/j.bbalip.2011.03.004